

**An integrated approach to the key parameters in methanol-to-olefins reaction catalyzed by MFI/MEL zeolite materials**

Liu, Chuncheng; Uslamin, Evgeny A.; van Vreeswijk, Sophie H.; Yarulina, Irina; Ganapathy, Swapna; Weckhuysen, Bert M.; Kapteijn, Freek; Pidko, Evgeny A.

**DOI**

[10.1016/S1872-2067\(21\)63990-6](https://doi.org/10.1016/S1872-2067(21)63990-6)

**Publication date**

2022

**Document Version**

Accepted author manuscript

**Published in**

Chinese Journal of Catalysis

**Citation (APA)**

Liu, C., Uslamin, E. A., van Vreeswijk, S. H., Yarulina, I., Ganapathy, S., Weckhuysen, B. M., Kapteijn, F., & Pidko, E. A. (2022). An integrated approach to the key parameters in methanol-to-olefins reaction catalyzed by MFI/MEL zeolite materials. *Chinese Journal of Catalysis*, 43(7), 1879-1893. [https://doi.org/10.1016/S1872-2067\(21\)63990-6](https://doi.org/10.1016/S1872-2067(21)63990-6)

**Important note**

To cite this publication, please use the final published version (if applicable).  
Please check the document version above.

**Copyright**

Other than for strictly personal use, it is not permitted to download, forward or distribute the text or part of it, without the consent of the author(s) and/or copyright holder(s), unless the work is under an open content license such as Creative Commons.

**Takedown policy**

Please contact us and provide details if you believe this document breaches copyrights.  
We will remove access to the work immediately and investigate your claim.

1           **An integrated approach to the key parameters in methanol-to-olefins**  
2                           **reaction catalyzed by MFI/MEL zeolite materials**

3    Chuncheng Liu,<sup>a,d</sup> Evgeny A. Uslamin,<sup>a</sup> Sophie H. van Vreeswijk,<sup>c</sup> Irina Yarulina,<sup>b</sup> Swapna  
4           Ganapathy,<sup>c</sup> Bert M. Weckhuysen,<sup>c</sup> Freek Kapteijn,<sup>d,\*</sup> Evgeny A. Pidko<sup>a,\*</sup>

5           a: Inorganic Systems Engineering, Department of Chemical Engineering, Delft University of  
6           Technology, Van der Maasweg 9, 2629 HZ Delft, the Netherlands.

7           b: BASF SE, Process Research and Chemical Engineering, 67056 Ludwigshafen, Germany

8    c: Inorganic Chemistry and Catalysis, Debye Institute for Nanomaterials Science, Utrecht University,  
9           Universiteitsweg 99, 3854 CG Utrecht, the Netherlands

10   d: Catalysis Engineering, Department of Chemical Engineering, Delft University of Technology, Van  
11           der Maasweg 9, 2629 HZ Delft, the Netherlands

12    Corresponding authors: [F.Kapteijn@tudelft.nl](mailto:F.Kapteijn@tudelft.nl) (FK); [e.a.pidko@tudelft.nl](mailto:e.a.pidko@tudelft.nl) (EAP)

13   **Abstract:** Identification of the catalyst characteristics correlating with the key performance  
14   parameters including selectivity and stability is key to the rational catalyst design. Herein we  
15   focused on the identification of property-performance relationships in the methanol-to-olefin  
16   (MTO) process by studying in detail the catalytic behaviour of MFI, MEL and their respective  
17   intergrowth zeolites. The detailed material characterization reveals that both the high  
18   production of propylene and butylenes and the large MeOH conversion capacity correlate with  
19   the enrichment of lattice Al sites in the channels of the pentasil structure as identified by <sup>27</sup>Al  
20   MAS NMR and 3-methylpentane cracking results. The lack of correlation between MTO  
21   performance and other catalyst characteristics, such as crystal size, presence of external  
22   Brønsted acid sites (BAS) and Al pairing suggests their less pronounced role in defining the  
23   propylene selectivity. Our analysis reveals that catalyst deactivation is rather complex and is  
24   strongly affected by the enrichment of lattice Al in the intersections, the overall Al-content, and  
25   crystal size. The intergrowth of MFI and MEL phases accelerates the catalyst deactivation rate.

1 **Keywords:** structure-performance relationships; zeolite catalysis; methanol-to-olefin  
2 conversion; Al-distribution; acidity; intergrowth MFI/MEL; pentasil

### 3 **1. Introduction**

4 The methanol-to-olefins (MTO) technology has the potential to play a major role in the  
5 sustainable production of light olefins. It is recognized as one of the key ingredients within the  
6 methanol (MeOH) economy concept [1, 2] enabling the production of the crucial hydrocarbon  
7 building blocks, such as light olefins, starting from CO<sub>2</sub> as the primary carbon source.[3]  
8 Despite the worldwide industrialization of the MTO process [4-6], intense research is still  
9 focusing on a better understanding of the underlying structure-performance relationship for the  
10 optimization of this catalytic process and the development of more selective and stable catalytic  
11 materials.[7-14] In particular, the growing demand for renewable propylene emphasizes the  
12 importance of further optimization of the selectivity of the MTO catalysts towards propylene  
13 production.

14 The mechanism of the MTO process is highly complex. A multitude of parallel and  
15 consecutive chemical transformations of the substrates are catalyzed by Brønsted acid sites  
16 (BAS) resulting in a range of hydrocarbon products.[15-19] After a rather short induction period,  
17 two catalytic cycles involving the interconversion of confined olefinic and aromatic  
18 intermediates promote simultaneously the MeOH conversion and the formation of longer-chain  
19 hydrocarbons.[20-23] The cracking of the olefinic intermediates in the so-called olefinic cycle  
20 is solely responsible for the formation of all olefinic products, with ethylene as exception which  
21 is also mainly produced via the dealkylation of larger aromatic intermediates within the  
22 aromatic cycle [7, 24].

23 The concentration, location, and distribution of Brønsted Acid Sites (BAS) are of primary  
24 importance to define the activity in the MTO process. By increasing the Al concentration, the  
25 chance of interaction between guest substrates and BAS simultaneously increases, eventually

1 promoting the aromatic cycle, increasing aromatics and ethylene formation.[25, 26] Zeolites  
2 with the same BAS density can also exhibit a substantially different MTO performance,  
3 ascribed to the heterogeneous distribution of Al within the crystal.[16] The presence of strong  
4 BAS on the external surface of zeolite crystallites was shown to promote coking and decreases  
5 the catalyst lifetime.[27] At high Al content when Al ions are in close vicinity, separated by  
6 two or more silicon tetrahedra, the so-called Al<sub>pair</sub> is formed. The cooperation of the BAS  
7 associated with such Al<sub>pair</sub> decreases the energy barrier for the formation of aromatic  
8 intermediates [28] eventually increasing the selectivity towards aromatic products at the  
9 expense of the selectivity towards propylene.

10 The relative rates of the two catalytic cycles also depend on the topological properties of  
11 the confined space, where the reaction takes place, and they determine the selectivity of the  
12 catalytic process. The uniform micropores of the zeolite catalyst ensure the efficient  
13 confinement and stabilization of the reaction intermediates (transition-state selectivity [29]),  
14 while the pore diameter only allows the products that fit to pass through and escape the zeolite  
15 (product-selectivity [29, 30]). Among more than 230 zeolite topologies, the 10-membered ring  
16 (10-MR) zeolites have attracted great interest in the MTO process.[31-35] Particularly, 10-MR  
17 TON-type zeolites consisting of 1-dimensional channels exhibit high selectivity towards C<sub>5+</sub>  
18 hydrocarbons with a negligible contribution of aromatics. Because of shape-selectivity the  
19 narrow channels (4.6 Å × 5.7 Å) host the key intermediates of the olefinic cycle, *e.g.*  
20 methylcyclopentenyl cations.[35, 36] However, the application of TON-type zeolites in the  
21 MTO process is hindered by fast deactivation, which is probably due to the rapid coke  
22 deposition easily blocking the 1D channels [32, 34, 35]. In this study, catalysts with zeolite  
23 topologies MFI (HZSM-5) and MEL (HZSM-11) of the pentasil family are investigated. These  
24 10-MR zeolite topologies display 3-dimensional channel and intersection systems with very  
25 similar diameters. While MFI-type zeolite consists of straight (4.5 Å) and sinusoidal (4.7 Å)

1 channels with intersection (6.4 Å), MEL-type consists of only straight channels (5.2 Å) with  
2 intersection (7.7 Å).[37] These single topologies are further compared with mixed-topology  
3 zeolite catalysts consisting of intergrown MFI and MEL crystal phases, indicated by HZBM-  
4 10. A detailed skeletal description of how MFI and MEL phases mix at an atomic scale is given  
5 in [38]. These 10-membered ring zeolites with 3-dimensional pores have been widely  
6 investigated because of the promising selectivity towards propylene and butylenes in MTO  
7 combined with the prolonged lifetime in comparison with 1-dimensional 10-MR zeolites.[31-  
8 33]

9 The comparative MTO study of MFI-type, MEL-type and TON-type zeolites by Hunger  
10 and co-workers [31] showed that under optimized conditions a comparable selectivity towards  
11 propylene (~50%) for MFI-type and MEL-type zeolites can be achieved at an optimal BAS  
12 density (~15 mmol/g), while the selectivity towards propylene is reduced to ~38% for TON-  
13 type zeolites (BAS ~30 mmol/g). The major conclusion was drawn that the BAS density is an  
14 important optimizing parameter for tuning the MTO selectivity, but did not provide insight in  
15 the relation with the structural properties of those zeolites. Fan and co-workers compared the  
16 MTO performance for MFI- and MEL-type zeolite catalyst and demonstrated that the MEL-  
17 type H-ZSM-11 is more selective to produce light olefins [33]. Furthermore, it was proposed  
18 that for the zeolites with a higher Si/Al ratio (>120), the lattice Al enrichment in the zeolite  
19 channels is the key factor that determines the MTO product selectivity. The use of materials  
20 featuring an intergrowth framework with mixing MFI and MEL topologies as an MTO catalyst  
21 was also shown to enhance the propylene selectivity in comparison with the pure MFI-based  
22 HZSM-5 catalysts.[39] By varying the composition of MFI or MEL phases in the zeolite, the  
23 MeOH selectivity to propylene could be increased to ca. 46% from 27% for MFI. There is a  
24 general consensus in the research community that shape selectivity, ascribed to the subtle  
25 differences in the geometry and structure of the zeolite confined space, is one of the key factors

1 that determines the MTO catalyst performance and, particularly, the selectivity towards  
2 propylene.[40] However, the different synthesis methods for different zeolite topologies and  
3 various post-synthesis approaches inevitably introduced the variation in other parameters  
4 including crystal morphology, Si/Al ratio, Al distribution (at internal or external surface, in  
5 channels or intersections), and potentially other physicochemical properties, which all may also  
6 substantially affect the catalyst behavior. Therefore, an integrated approach for analysing all  
7 these parameters is crucial to find out the key parameter(s) to control the catalytic performance.  
8 A thorough analysis of the possible correspondence thereafter will lead to a comprehensive  
9 structural-performance relationship.

10 In this study a systematic analysis of all the above-mentioned aspects is performed in an  
11 attempt to identify in a comprehensive approach the key descriptor(s) that intrinsically control(s)  
12 the MTO performance of the 10-MR zeolites under study, namely HZSM-5, HZSM-11 and an  
13 intergrowth phase HZBM-10. With this in mind, steady-state MTO tests combined with  
14 *operando* UV–vis spectroscopy measurements firstly emphasized the different catalytic  
15 behaviors with respect to selectivity, MTO stability, and various features on the surface of  
16 MEL-type, MFI-type, and the intergrowth zeolites. Through a wide range of characterization,  
17 spectroscopic measurements, and probe reactions, substantial differences were highlighted on  
18 the crystal size, BAS distribution over the crystal, Al<sub>pair</sub>, and Al-siting of all tested zeolites.  
19 Combined with the MTO selectivity and stability, the correlation between each of the  
20 parameters and the catalytic performance was thoroughly evaluated and discussed. The  
21 significance of each parameter on the product selectivity and lifetime was eventually addressed.

## 2. Experimental methods

### 2.1 Chemicals

All reagents were of reagent grade and used without further purifications: sodium nitrate ( $\text{NaNO}_3$ , Sigma Aldrich, ACS reagent,  $\geq 99.0\%$ ), cobalt(II) nitrate hexahydrate (Alfa Aesar, ACS reagent, 98.0-102.0%), 1,3,5-triisopropylbenzene (1,3,5-TIPB, Sigma Aldrich, 95%), 3-methylpentane (3-MP, Alfa Aesar, 99+%), *n*-hexane (Sigma-Aldrich, 99%), 2,4-dimethylquinoline (2,4-DMQ, Alfa Aesar, 95%), methanol (MeOH, Sigma-Aldrich, for HPLC,  $\geq 99.9\%$ ) and deionized water.

### 2.2 Zeolite materials

Zeolite samples with different topologies including MFI (ZSM-5), MEL (ZSM-11), and intergrowth MFI/MEL (ZBM-10) were obtained from commercial sources. ZSM-5 samples with different Si/Al ratio and crystal size including CBV5020E (Zeolyst Int., Si/Al=25), BASF1 (BASF, Si/Al=25) and BASF2 (BASF, Si/Al=50) are denoted by MFI-25-M, MFI-25-S and MFI-50-S, respectively (S and M indicate the respective small and medium crystal size based on scanning electron microscope (SEM) and X-ray powder diffraction (XRD) analysis). ZSM-11 samples were purchased from ACS Material (MZ110012, Si/Al=25) denoted as MEL-25-S. Two intergrowth zeolite samples ZBM-10 featuring different crystal sizes were provided by BASF and named as MFI/MEL-25-S and MFI/MEL-50-L, where S and L represent samples with respective small and large crystal size. All the above-mentioned zeolite samples were calcined in air at 550 °C (2 °C/min) for 6 h to obtain the protonic form.

### 2.2 Chemical composition, structural and textural properties

The chemical composition of zeolite materials was assessed with ICP-AES (Inductively coupled plasma atomic emission spectroscopy) using a Perkin Elmer Optima 5300DV

1 instrument (glass torch + saffire injector). Prior to measurement, 50 mg zeolite sample was  
2 digested in 4.5 mL 30% HCl + 1.5 mL 65% HNO<sub>3</sub> + 0.2 mL 40% HF using microwave heating  
3 for ca. 60 min. The resulting solutions were then diluted to 50 mL with deionized water.

4 X-ray powder diffraction (XRD) was performed in Bragg-Brentano geometry with a Bruker  
5 D8 Advance X-ray diffractometer using monochromatic Co K $\alpha$  ( $\lambda = 1.788970 \text{ \AA}$ ) radiation  
6 between  $2\theta = 5^\circ$  and  $55^\circ$ . The refinement and quantitative phase analysis were carried out using  
7 Topas software. The crystal size analysis was carried out by applying the Scherrer method:

$$8 \quad D = \frac{K \times \lambda}{B \times \cos \theta}$$

9 where  $D$  represents the diameter of a spherical nanocrystal with  $K = 0.89$ ,  $\lambda$  is the wavelength  
10 of X-ray,  $\theta$  is the diffraction angle of the band at  $9.2^\circ$ , and  $B$  is the corrected half width of the  
11 observed half width considering the instrumental impact.

12 Microporous properties of each sample were assessed from N<sub>2</sub> physisorption isotherms  
13 at  $-196^\circ \text{C}$  using Tristar II 3020. Prior to the measurements, samples were dried and degassed  
14 at  $350^\circ \text{C}$  for 6 h under constant N<sub>2</sub> flow.

15 X-ray Photoelectron Spectroscopy (XPS) was employed to determine the Si/Al ratio on the  
16 outer surface of the tested zeolites. XPS spectra were collected using a Thermo Scientific K-  
17 alpha spectrometer equipped with a monochromatic Al K $\alpha$  X-ray source and a  $180^\circ$  double-  
18 focusing hemispherical analyser with a 128-channel detector.

### 19 ***2.3 Acid site density and Al distribution***

#### 20 ***FTIR Pyridine adsorption***

21 Transmission FT-IR spectroscopy of adsorbed pyridine as a probe molecule was used to  
22 quantify the acid site density of the catalytic materials (MFI-25-S as reference estimated from  
23 formula: H<sub>n</sub>Al<sub>n</sub>Si<sub>96-n</sub>O<sub>192</sub>·16H<sub>2</sub>O,  $n = 3.7$ ). Samples (20 mg) were pressed in self-supported



1 wafers with diameter 1.6 cm and then placed in an IR quartz cell. The spectra were collected at  
2  $2\text{ cm}^{-1}$  resolution using a Nicolet Nexus spectrometer equipped with an extended KBr beam  
3 splitting and an MCT detector. The amount of BAS and LAS was derived from the absorbance  
4 at 1545 and 1456  $\text{cm}^{-1}$  using the integrated molar extinction coefficients of 0.73 and 1.11,  
5 respectively.[41] Assuming that one pyridine molecule is only adsorbed on one BAS/LAS, the  
6 following equations were used to estimate  $C_{\text{BAS}}$  and  $C_{\text{LAS}}$ :

$$7 \quad C_{\text{BAS}} = 4.30 \times IA(\text{BAS})R^2 / W$$

$$8 \quad C_{\text{LAS}} = 2.83 \times IA(\text{LAS})R^2 / W$$

9 where  $IA$  ( $\text{BAS}$ ,  $\text{LAS}$ ) represents the integrated absorbance of the band at 1545 and 1456  $\text{cm}^{-1}$ ,  
10  $R$  is the radius of sample wafer (cm) and  $W$  is the weight of sample wafer (g).

### 11 ***FTIR of adsorbed CO***

12 To compare the strength of these acid sites, transmission FT-IR spectra with CO as probe was  
13 carried out at  $-140\text{ }^\circ\text{C}$ . 10 mg powder was pressed in a self-supported wafer with diameter 0.8  
14 cm. After pre-treating at  $400\text{ }^\circ\text{C}$  overnight under vacuum, IR spectra were collected at  $2\text{ cm}^{-1}$   
15 resolution using a Nicolet Nexus spectrometer within  $400\text{--}4000\text{ cm}^{-1}$ . During spectra collection,  
16 liquid nitrogen is used to maintain the IR cell temperature at ca.  $-140\text{ }^\circ\text{C}$ . The partial pressure  
17 of CO was stepwise increased (0.1 mbar per step) through a manifold connected to the specimen  
18 holder.

### 19 ***Solid state magic angle spinning (MAS) NMR measurements***

20 Solid state magic angle spinning (MAS) NMR measurements of fully hydrated samples were  
21 performed on a Bruker Ascend 500 magnet (11.7 T) equipped with a NEO console operating at  
22 a  $^{27}\text{Al}$  resonance frequency of 130.32 MHz, using a Bruker 3.2 mm two channel MAS probe  
23 head. The MAS rate was set to 20 kHz for all measurements. To obtain the high-resolution  $^{27}\text{Al}$   
24 MAS NMR spectrum for quantitative analysis of Al distribution, the single pulse  $^{27}\text{Al}$  MAS

1 NMR measurements were recorded with a pulse length of 1.25  $\mu\text{s}$ , a recycle delay of 0.5 s, and  
2 10240 scans each.[42] Two-dimensional (2D) multiple quantum magic-angle spinning (MQ  
3 MAS) NMR spectra were measured using a triple quantum z-filter pulse sequence. Excitation  
4 and conversion pulses of 3.4  $\mu\text{s}$  and 1.1  $\mu\text{s}$  and a selective soft pulse of 11  $\mu\text{s}$  for the z-filter  
5 filtering were utilized. All 2D spectra consist of 100 transients, each transient incremented by  
6 70  $\mu\text{s}$  with a recycle delay of 0.2 s. Five characteristic peaks with fixed width at 58 ppm, 56  
7 ppm, 55 ppm, 53 ppm and 52 ppm were used for 1D  $^{27}\text{Al}$  MAS NMR spectra deconvolution  
8 using Voigt function [43, 44] ( $G/L = 0.5$  [45]).[33, 42, 46]

### 9 *Co(II) ion exchange and UV–vis diffuse reflectance spectra measurements*

10 To analyze the distribution of Al atoms (including  $\text{Al}_{\text{pair}}$  and  $\text{Al}_{\text{single}}$ ) locations in the zeolite  
11 framework, UV–vis diffuse reflectance spectra (UV–vis-DRS) of fully Co-exchanged zeolites  
12 were measured on a Perkin-Elmer Lambda 900 spectrophotometer equipped with an integrating  
13 sphere (“Labsphere”) using  $\text{BaSO}_4$  as a reference. Before measurement, the protonic zeolites  
14 were exchanged 3 times with 200 mL of 1M  $\text{NaNO}_3$  solution per 1 g zeolite at 70  $^\circ\text{C}$ . After  
15 recovering by centrifugation, Co ion exchange was then performed with 100 mL 0.05M  
16  $\text{Co}(\text{NO}_3)_2$  solution per 1 g zeolite at room temperature under stirring for 24 h. The exchange  
17 was repeated three times with centrifugation between each repetition.[47] Washed by deionized  
18 water after the third ion exchange, the obtained Co(II)-exchanged samples were then dried at  
19 room temperature under dynamic vacuum and then dehydrated at 400  $^\circ\text{C}$  under constant  $\text{N}_2$   
20 flow for 7 h before being transferred to the self-sealing UV–vis sample holder in a moisture-  
21 free glovebox.[48-50] The absorption intensity is expressed by the Schuster-Kubelka-Munk  
22 equation:

$$23 \quad F(R_\infty) = (1 - R_\infty)^2 / 2R_\infty$$

24 The distribution of Al atoms in the zeolite framework is categorized as  $\text{Al}_{\text{pair}}$  and  $\text{Al}_{\text{single}}$  as  
25 reported by Dědeček *et al.*[47] Co(II) cations are selectively exchanged on  $\text{Al}_{\text{pair}}$  sites under the

1 above-mentioned conditions.[51] Combined with the amount of Na ions remaining in the  
2 framework after Co(II) ion exchange, the number of  $Al_{pair}$  and  $Al_{single}$  can be calculated as below:

$$3 \quad Al_{single} = [Na]$$

$$4 \quad Al_{pair} = 2 \times [Co]$$

$$5 \quad Al_{framework} = [Na] + 2 \times [Co]$$

6 where  $[Co]$  and  $[Na]$  represent concentrations of  $Co^{2+}$  and  $Na^+$  in the sample determined by  
7 ICP-AES after Co ion exchange.

### 8 ***Cracking of 1,3,5-triisopropylbenzene (1,3,5-TIPB)***

9 To probe the external BAS, cracking of 1,3,5-TIPB was used as a probe reaction.[52, 53] The  
10 catalytic tests were conducted in a fixed bed reactor. 20 mg catalyst (150–212  $\mu m$ ) was activated  
11 at 550 °C in 50 mL/min air before reaction at 200 °C. 1,3,5-TIPB in low concentration (0.3 %  
12 v/v) was fed with 50 mL/min  $N_2$  after passing through a saturator at 10 °C.

### 13 ***Cracking of 3-methylpentane (3-MP) and n-hexane***

14 To probe the Al-arrangement (channel versus intersection) in the zeolite framework [33, 42],  
15 the cracking of 3-MP was used as a probe reaction conducted in a fixed bed reactor.[54] In a  
16 typical experiment, 20 mg catalyst (150–212  $\mu m$ ) was activated at 550 °C in 50 mL/min air  
17 prior to reaction at 400 °C. 2,4-Dimethyl quinoline (2,4-DMQ) base was added to deactivate  
18 surface sites.[52] To control total conversion below 10%, the partial pressure of 3-MP was  
19 adjusted at 3.8 kPa by passing 50 mL/min  $N_2$  as carrier gas through a saturator at 5°C. Hydrogen,  
20 methane and ethane are selectively formed through the monomolecular cracking of the  
21 pentacoordinated carbonium ion formed by the protonation of the 3-MP molecule on the BAS  
22 inside the zeolite crystals. In contrast, the energetically favourable bimolecular cracking [55]  
23 via primary carbenium ions would require a more spacious space to hold the bulkier transition  
24 state of 3-MP and forms mainly only hydrocarbons beyond C3. A previous study found that the

1 bimolecular cracking can hardly occur on H-ZSM-22, which displays the 1-dimensional  
2 straight 10-MR channels without intersections.[42] Thus, the selectivity towards the cracking  
3 products hydrogen, methane and ethane (moles / 100 mol cracked) is a good indicator of  
4 monomolecular cracking of 3-MP solely on BAS located in the straight or sinusoidal channels.

$$5 \quad S_{H_2+CH_4+C_2H_6} = \frac{\phi_{CH_4} + \phi_{C_2H_6} + \phi_{H_2}}{\phi_{3-MP_{in}} - \phi_{3-MP_{out}}} \cdot 100,$$

6 where  $\phi_{C_n}$  and  $S$  represents the molar flow rate and selectivity in unit of moles per 100 mol 3-  
7 MP cracked, respectively.

8 Constraint index (CI) is used to evaluate the steric hindrance of a zeolite topology upon the  
9 reactant and represents the ratio of the (assumed) first order rate constants of  $n$ -hexane and 3-  
10 MP cracking.[56] To measure CI for studied materials, a 4 mm (ID) quartz tube reactor was  
11 filled with 20 mg sieved zeolite fraction (particle size 150–212  $\mu\text{m}$ ).  $n$ -Hexane and 3-MP were  
12 simultaneously fed into the reactor using 10 mL/min He as carrier passing through a saturator  
13 containing a mixture of  $n$ -hexane and 3-MP at 11°C. The reaction was performed at 400°C in  
14 the presence of 2,4-DMQ to deactivate surface sites.[52]. The CI value is calculated as:

$$15 \quad CI = \frac{k_{n\text{-hexane}}}{k_{3\text{-MP}}} = \frac{\ln(1 - X_{n\text{-hexane}})}{\ln(1 - X_{3\text{-MP}})}$$

## 16 **2.4 Catalytic performance testing**

17 MTO reactions were performed at 450 °C using a fixed-bed reactor setup. A 4 mm (ID) quartz  
18 tube reactor was filled with 40 mg sieved zeolite fraction (particle size 150–212  $\mu\text{m}$ ). MeOH  
19 was fed into the reactor using a thermostated saturator with liquid MeOH and  $\text{N}_2$  as a carrier  
20 gas. The reaction products were analysed with an online Thermo Trace GC equipped with a  
21 thermal conductivity detector (TCD) coupled with a PoraPLOT Q pre-column (2 m, 0.32 mm,  
22 20  $\mu\text{m}$ ) and Molsieve 5A column (10 m, 0.32 mm) for analysis of permanent gases, a flame  
23 ionization detector (FID) equipped with RTX-1 column (2 m, 0.32 mm, 5.00  $\mu\text{m}$ ) and

1 Al<sub>2</sub>O<sub>3</sub>/KCl column (15 m, 0.32 mm, 10 μm) for the analysis of C<sub>1</sub> to C<sub>4</sub> hydrocarbons and the  
2 other FID equipped with RTX-VMS column (30 m, 0.33 mm, 3.00 μm) for C<sub>5+</sub> hydrocarbons.

3 Prior to reaction, the catalyst was activated in 50 mL/min air by heating up at 5 °C/min to  
4 550 °C and then cooling down to the reaction temperature 450 °C. The partial pressure of  
5 MeOH in the flow was set at 5.2 kPa, corresponding with a weight hourly space velocity  
6 (WHSV) of 5.2 g<sub>MeOH</sub>g<sub>cat</sub><sup>-1</sup>h<sup>-1</sup>. The reaction conversion, selectivity and yield were then  
7 calculated on a carbon molar basis as follows:

$$8 \quad X = \frac{\phi_{C,MeOH_{in}} - \phi_{C,MeOH_{out}} - 2\phi_{C,DME_{out}}}{\phi_{C,MeOH_{in}}} \cdot 100\%;$$

$$9 \quad S_{Cn} = \frac{n \cdot \phi_{Cn}}{\phi_{C,MeOH_{in}} - \phi_{C,MeOH_{out}} - 2\phi_{C,DME_{out}}} \cdot 100\%;$$

$$10 \quad Y_{Cn} = \frac{X \cdot S_{Cn}}{100},$$

11 where  $X$ ,  $\phi_{Cn}$ ,  $S_{Cn}$  and  $Y_{Cn}$  represent the carbon-based conversion of MeOH plus dimethyl ether  
12 (DME), molar flow rate and carbon selectivity to certain hydrocarbon product in the exhaust  
13 with carbon number equal to  $n$  and the corresponding carbon yield, respectively. To describe  
14 the catalyst deactivation, MeOH conversion capacity [57] was estimated following:

$$15 \quad R_0 = WHSV_{MeOH} \times t_{0.5},$$

16 where  $WHSV_{MeOH}$  is the weight hourly space velocity of MeOH and  $t_{0.5}$  is the catalyst lifetime  
17 with MeOH conversion is within 100–50%.

18 After catalytic tests, thermogravimetric analysis of the spent catalyst samples was  
19 performed on a Mettler Toledo TGA/SDTA 851e TGA analyser. 20 mg Spent catalyst was first  
20 treated at 200 °C with 20 mL/min air for 1 h to remove water and other volatile species, and  
21 then heated in the same air flow up to 800 °C at 5 °C/min while recording the sample mass.

## 1        **2.5 Operando UV–vis diffuse reflectance spectroscopy**

2        Operando UV–vis diffuse reflectance spectra were collected using 60 mg of sieved catalyst  
3        (particle size 212–355  $\mu\text{m}$ ) in a quartz, rectangular reactor. Details of the set-up can be found  
4        elsewhere.[58-60] Prior to reaction and spectra collection, the catalyst was pre-treated at 550  $^{\circ}\text{C}$   
5        in 10 mL/min  $\text{O}_2$  for 1 h after which a He flow of 35 ml/min was used to get rid of the  $\text{O}_2$ . The  
6        MTO reaction was carried out at 450  $^{\circ}\text{C}$  by flowing He as a carrier gas (25 mL/min) through a  
7        MeOH saturator kept at 21  $^{\circ}\text{C}$ , corresponding with a WHSV of  $\sim 5.4 \text{ g}_{\text{MeOH}}\text{g}_{\text{cat}}^{-1}\text{h}^{-1}$ . During  
8        MeOH conversion, *operando* UV–Vis spectra were obtained using an AvaSpec 2048L  
9        spectrometer connected to a high-temperature UV–Vis optical fiber probe, which was used to  
10       collect spectra in reflection mode. Every minute a spectrum was saved with 100 accumulations  
11       of 80 ms exposure time.

12

### 3. Results and discussion

#### 3.1 Physicochemical Properties

**Figure 1** shows the representative XRD patterns for all zeolite materials together with Rietveld refinement and quantitative results in **Table S1**. XRD patterns of pure MFI samples and MEL-25-S show close agreements with the expected reflections of MFI and MEL phases, respectively.[37] In comparison with MFI samples, the increasing ratio of intensity between the (0 1 3) reflection at  $23.7^\circ$  and the (2 4 1) reflection at  $24.3^\circ$  in MFI/MEL-25-S and MFI/MEL-50-L confirms the presence of the MEL in the intergrowth samples.[39] The refinement in **Table S1** gives the unit cell parameters of all catalysts, which correspond well with the reported values.[37] The XRD data indicate a high crystallinity of all the utilized materials. The crystallinity fraction shows that MFI/MEL-25-S contains 50%/50% of MFI and MEL phase, while MFI/MEL-50-L contains 63%/37% of MFI and MEL phase.

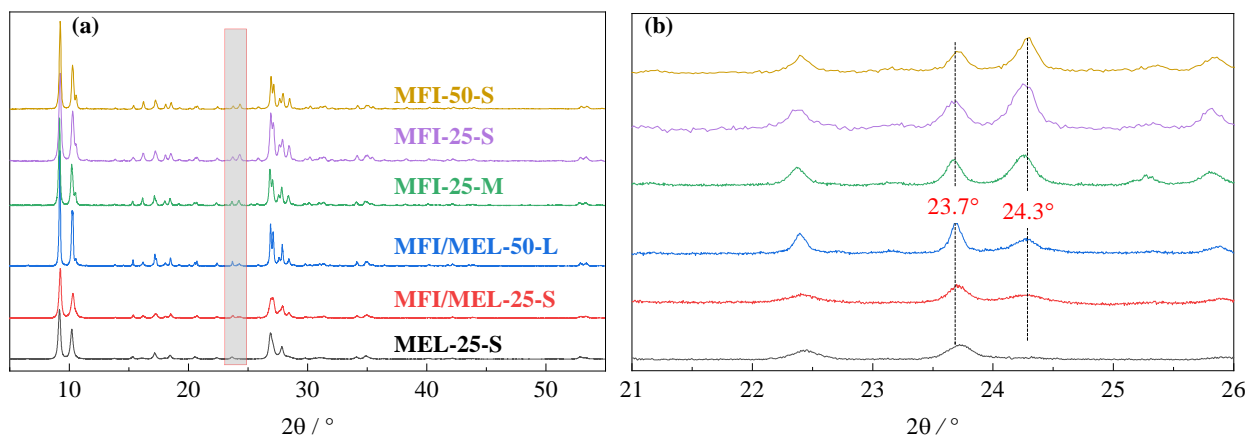


**Figure 1.** X-ray diffraction data comparing patterns for investigated samples (a), and a highlighted 21–26° range (b).

The textural and acidic characteristics of the zeolite catalysts are summarized in **Table 1**. The chemical compositions give the actual Si to Al ratio in agreement with that as provided. The SEM results (**Figure S1**) show that intergrowth MFI/MEL-50-L consists of the largest

1 aggregates with a diameter of 2–5  $\mu\text{m}$  while the other zeolites feature particle sizes below 1  $\mu\text{m}$ .  
2 All samples have a similar micropore volume of 0.15–0.16  $\text{cm}^3\text{g}^{-1}$  resulting in similar  $\text{N}_2$   
3 adsorption isotherms at  $P/P^0 < 0.6$  (**Figure S2**). The smallest external surface area (27  $\text{m}^2\text{g}^{-1}$ )  
4 is observed for the MFI/MEL-50-L featuring largest crystal size (830  $\text{\AA}$ , **Table 1**). The steep  
5 uptake of  $\text{N}_2$  from  $P/P^0 > 0.7$  without an evident hysteresis loop on the samples with the ‘S’  
6 suffix is in line with the developed external surface area of the smaller-crystallite materials. As  
7 a consequence,  $V_{\text{total}}$ , which is evaluated on the isotherm point at  $P/P^0 = 0.95$  shows that samples  
8 with the small crystal size exhibit the larger amount of  $\text{N}_2$  adsorbed of 0.28–0.31  $\text{cm}^3\text{g}^{-1}$  than  
9 MFI-25-M (0.22  $\text{cm}^3\text{g}^{-1}$ ) and MFI/MEL-50-L (0.19  $\text{cm}^3\text{g}^{-1}$ ). These results together with the  
10 XRD data show that the crystal size varies as follows MFI/MEL-50-L > MFI-25-M > MFI-25-  
11 S  $\approx$  MFI-50-S  $\approx$  MEL-25-S  $\approx$  MFI/MEL-25-S.

12 The acidic properties of the catalysts assessed by FTIR spectroscopy of adsorbed pyridine  
13 confirm that the concentrations of BAS in the Si/Al=25 and =50 samples are consistent with  
14 their chemical compositions, while MFI/MEL-25-S contains a higher density of Lewis acid  
15 sites (LAS) than the others. The strength of BAS was assessed by FTIR of adsorbed CO. Upon  
16 interacting with CO, the downward shift in the OH stretching frequency and the upward shift  
17 in the CO vibrations are directly related to the strength of BAS.[61] As shown in **Figure S4**, a  
18 similar  $\Delta\nu(\text{OH})$  (310–314  $\text{cm}^{-1}$  in Si/Al = 25 and 313–317  $\text{cm}^{-1}$  in Si/Al = 50) is observed.  
19 Together with the similar C-O stretching shift (35–36  $\text{cm}^{-1}$  in Si/Al = 25 and 36–37  $\text{cm}^{-1}$  in  
20 Si/Al = 50), it indicates an almost identical strength of the BAS for all studied samples.[61-64]  
21 BAS with slightly higher strength was characterized for MFI-50-S and MFI/MEL-50-L, which  
22 is ascribed to the lower Al concentration in those materials.[65, 66]

23



1 **Table 1.** Summarized textural and acidic properties of studied catalysts.

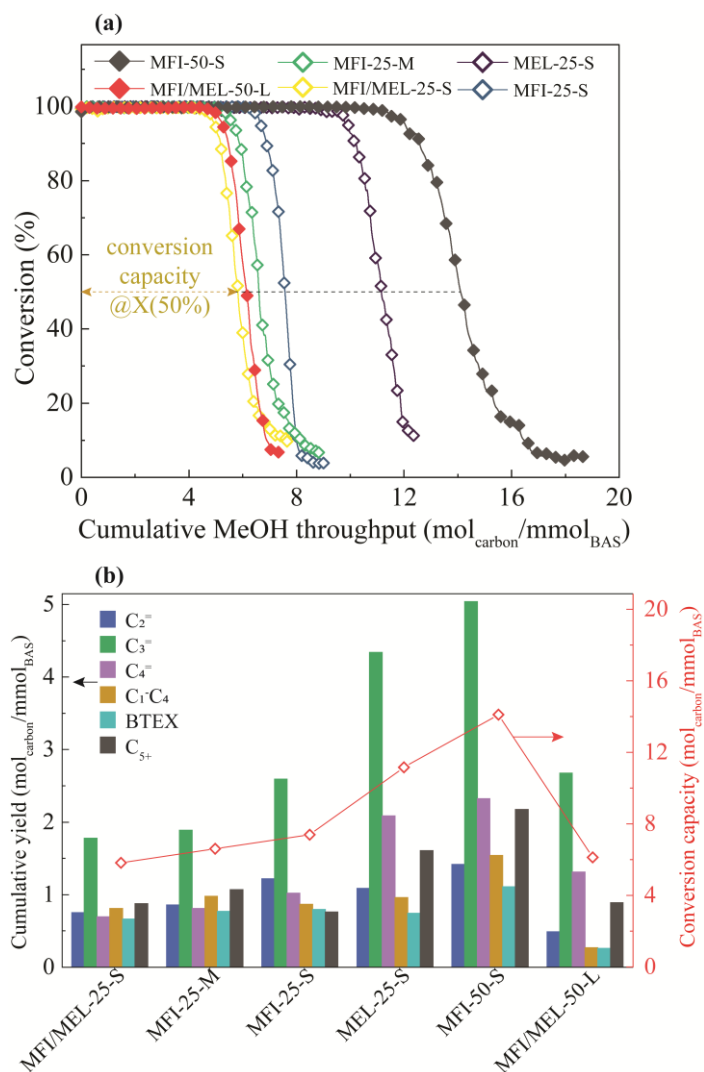
	Si/Al <sup>a</sup> (mol mol <sup>-1</sup> )	size <sup>b</sup> (Å)	V <sub>total</sub> <sup>c</sup> (cm <sup>3</sup> g <sup>-1</sup> )	V <sub>micro</sub> <sup>c</sup> (cm <sup>3</sup> g <sup>-1</sup> )	S <sub>ext</sub> <sup>c</sup> (m <sup>2</sup> g <sup>-1</sup> )	S <sub>BET</sub> <sup>d</sup> (m <sup>2</sup> g <sup>-1</sup> )	BAS <sup>e</sup> (μmolg <sup>-1</sup> )	LAS <sup>e</sup> (μmolg <sup>-1</sup> )
MEL-25-S	27	419	0.31	0.14	85	439	543	90
MFI/MEL-25-S	25	463	0.31	0.15	81	448	556	139
MFI-25-M	26	613	0.22	0.17	56	414	575	94
MFI-25-S	25	428	0.27	0.16	67	453	530	74
MFI/MEL-50-L	48	830	0.19	0.16	27	423	376	72
MFI-50-S	50	428	0.29	0.16	77	471	338	91

2 <sup>a</sup>Molar ratio determined by ICP-AES. <sup>b</sup>From crystal size analysis on the XRD pattern within 8.4–9.8° by  
 3 applying the Scherrer equation. <sup>c</sup>From N<sub>2</sub> adsorption isotherms (**Figure S2**) using the t-plot method. <sup>d</sup>From N<sub>2</sub>  
 4 adsorption isotherms using the BET method. <sup>e</sup>Concentrations of BAS and LAS derived from FT-IR spectroscopy  
 5 analysis with pyridine as probe (**Figure S3**).

### 6 **3.2 Catalytic Testing**

7 To evaluate the MTO catalytic performance at steady-state conditions, the overall MTO activity  
 8 and deactivation as defined by cumulative production yields and MeOH conversion capacity  
 9 [57], for all materials are summarized in **Figure 2**. For all catalysts, the main products are  
 10 categorized into light olefins (ethylene C<sub>2</sub><sup>-</sup>, propylene C<sub>3</sub><sup>-</sup> and butylenes C<sub>4</sub><sup>-</sup>), C<sub>1</sub>-C<sub>4</sub> (methane,  
 11 ethane, propane and butanes), BTEX (benzene, toluene, ethylbenzene and xylenes), and C<sub>5+</sub> for  
 12 undefined hydrocarbons with carbon number higher than 4.

13 At the initial stage of the reaction full MeOH conversion is achieved. With the increase in  
 14 cumulative MeOH throughput all catalysts deactivate giving rise to a rapid decrease in  
 15 conversion due to coke deposition blocking zeolite micropores and the active sites.[67] For all  
 16 catalysts, except for the shorter lived MFI/MEL-50-L, the propylene selectivity remains  
 17 constant with TOS till MeOH conversion starts decreasing as shown in **Figure S5**. On the other  
 18 hand, the selectivities to ethylene and BTEX gradually decrease with TOS before MeOH  
 19 conversion drops. The similar profiles of ethylene and aromatics (BTEX) within the 100%  
 20 MeOH conversion range further support the mechanistic proposal by Olsbye *et al.* on the role  
 21 of the aromatics-based cycle for ethylene production.[7]



1  
 2 **Figure 2.** MeOH conversion as a function of cumulative MeOH throughput (a) and  
 3 cumulative carbon yields of different hydrocarbons until MeOH conversion is at 50% (color  
 4 bars) and estimated conversion capacity (symbols to right axis) (b) for all studied catalysts in  
 5 MTO tests. Reaction conditions:  $T = 450\text{ }^{\circ}\text{C}$ ,  $m_{\text{cat}} = 40\text{ mg}$  (150–212  $\mu\text{m}$ ), 1 bar,  $WHSV = 5.2$   
 6  $\text{g}_{\text{MeOH}}\text{g}_{\text{cat}}^{-1}\text{h}^{-1}$ , carrier gas  $\text{N}_2 = 50\text{ mL/min}$ . The full picture of MeOH conversion and product  
 7 selectivity curves as a function of time on stream (TOS) are presented in **Figure S5**.

8 The MeOH conversion capacity of MFI-50-S is  $14.1\text{ mol}_{\text{carbon}}\text{mmol}_{\text{BAS}}^{-1}$ , which is higher  
 9 than  $7.4\text{ mol}_{\text{carbon}}\text{mmol}_{\text{BAS}}^{-1}$  obtained over MFI-25-S, emphasizing the positive impact of the  
 10 lower Al concentration on the catalyst stability.[15] Regarding the crystallite size, MFI-25-M  
 11 with relatively larger crystal sizes exhibits a slightly lower conversion capacity (6.6

1 mol<sub>carbon</sub>mmol<sub>BAS</sub><sup>-1</sup>) than its counterpart MFI-25-S (7.4 mol<sub>carbon</sub>mmol<sub>BAS</sub><sup>-1</sup>). This is in line with  
2 previous observations that mesoporosity development, achieved by either synthesizing nano-  
3 sized zeolites or introducing a hierarchical structure, improves the catalyst stability in the MTO  
4 process.[68-71]. The intergrowth MFI/MEL-25-S and MFI/MEL-50-L catalysts show the  
5 lowest MeOH conversion capacity (ca. 5.8 and 6.1 mol<sub>carbon</sub>mmol<sub>BAS</sub><sup>-1</sup>, respectively) suggesting  
6 the intergrowth of the two zeolite phases increases the catalyst deactivation rate.

7 The product distributions in the MTO test are evaluated based on the cumulative yields  
8 (**Figure 2(b)**) and the carbon selectivity at varying MeOH conversion levels (**Figure 3** and  
9 **Figure S6**). Previous studies suggest the decrease in conversion in the later stage of the MTO  
10 test (gradual deactivation) can be regarded as the change in contact time due to the coke  
11 deposition particularly for MFI-type and TON-type zeolites.[57, 72, 73]

12 For all catalysts, the cumulative yields of propylene and butylenes are higher than other  
13 products (**Figure 2(b)**), which suggests the olefinic cycle reactions prevail over all materials at  
14 studied MTO conditions. Similar to the trend in the MeOH conversion capacity, MEL-25-S has  
15 the higher cumulative yield of propylene (4.3 mol<sub>carbon</sub>mmol<sub>BAS</sub><sup>-1</sup>) than MFI-25-S, MFI-25-M  
16 and MFI/MEL-25-S (2.6, 1.9, and 1.8 mol<sub>carbon</sub>mmol<sub>BAS</sub><sup>-1</sup>, respectively) with Si/Al of 25. A  
17 similar trend was also observed for samples with Si/Al of 50 emphasizing the impact of catalyst  
18 stability on the cumulative yields in the MTO process.

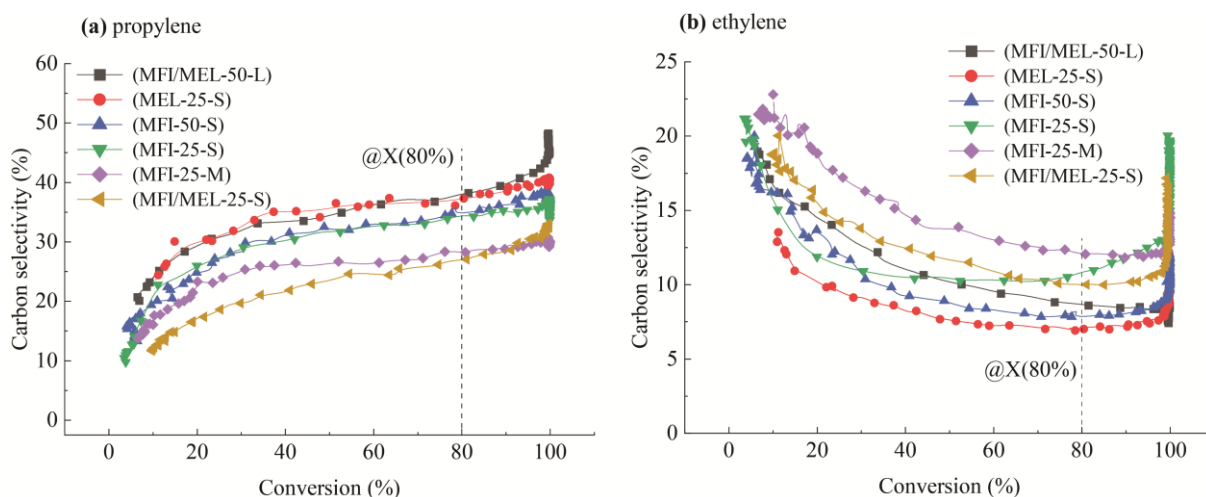


**Figure 3.** Carbon selectivity to propylene (a) and ethylene (b) as a function of MeOH

conversion over studied materials. Reaction conditions: Reaction conditions:  $T = 450\text{ }^{\circ}\text{C}$ ,  $m_{\text{cat}} = 40\text{ mg}$  (150–212  $\mu\text{m}$ ), 1 bar,  $WHSV = 5.2\text{ g}_{\text{MeOH}}\text{g}_{\text{cat}}^{-1}\text{h}^{-1}$ , carrier gas  $\text{N}_2 = 50\text{ mL/min}$ .

Similar graphs of other product groups are presented in **Figure S6**.

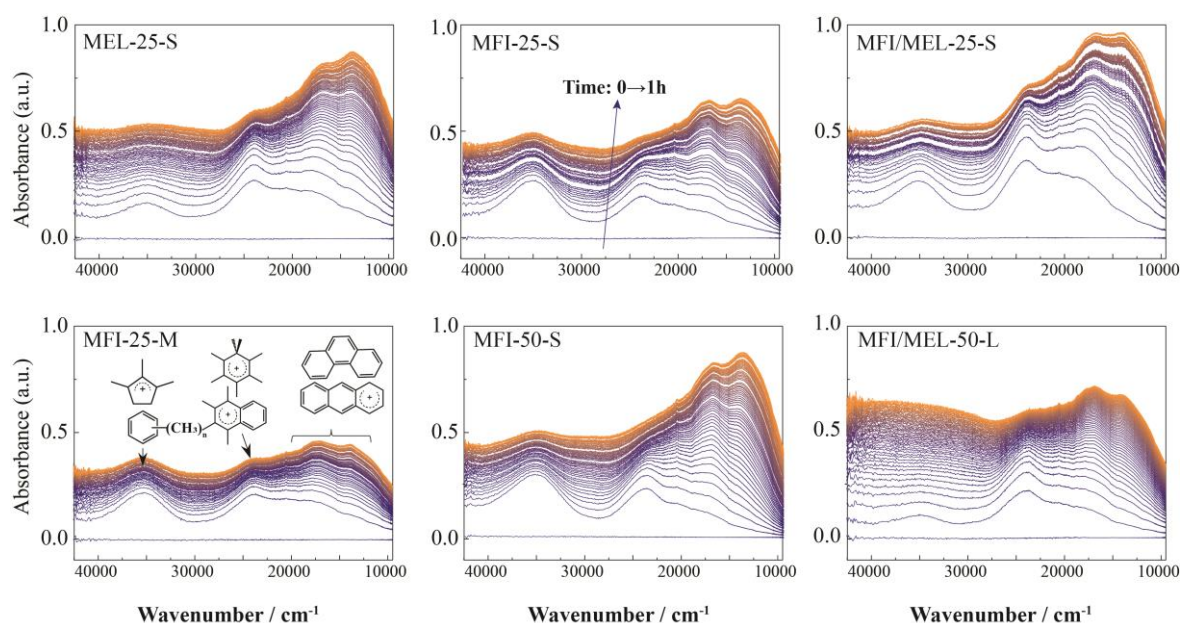
Upon decreasing MeOH conversion, the selectivity to propylene and butylene decreases while that to ethylene gradually increases (**Figure 3** and **S6**). The latter can be interpreted that more polyaromatic precursors present in the catalyst during the deactivation proceeds the dealkylation to give the ethylene formation. To note, the trends of selectivity towards propylene and ethylene are similar for all catalysts. Only the selectivity to ethylene over MFI-25-S, deviates from this general trend, showing no increase but a more constant level over a MeOH conversion of 80–20%. This correlates with the decreasing BTEX over that range in contrast to the more constant level for the other samples (**Figure S6**). Focusing on the comparison of product distribution over studied materials, the selectivity at MeOH conversion of 80% is chosen as reference in this study.

The selectivity to propylene is 27% and 38% for MFI/MEL-25-S and MFI/MEL-50-L, and 10% and 9% to ethylene, respectively. This is in line with earlier reports showing that a higher lattice Al concentration in MFI enhances the interaction of substituted benzene intermediates

1 with BAS giving rise to the propagation of the aromatics-based cycle and, accordingly, an  
2 increased ethylene and BTEX selectivity in the MTO process.[25] In a previous study the total  
3 light olefin selectivity in MTO was observed to monotonically increase with the crystal size,  
4 attributed to diffusion interference and a higher retention of methylbenzenes [74]. This latter is  
5 in line with a higher selectivity to ethylene of MFI-25-M than MFI-25-S in our study. Overall,  
6 the observed differences in selectivity levels for the different samples (**Figure 3**) point to the  
7 importance of other intrinsic catalyst characteristics that define the performance and selectivity  
8 of the MTO catalysts.

### 9 **3.3 Operando UV–vis Spectroscopy**

10 The active hydrocarbons formed from MeOH and then retained in the zeolite frameworks are  
11 defined as the hydrocarbon pool intermediates.[75, 76] During the MTO test, *operando* UV–  
12 vis spectra of the catalyst were recorded to follow the formation of the retained hydrocarbons.  
13 The results are displayed in **Figure 4**.



14  
15 **Figure 4.** Time-resolved operando UV–vis spectra during MeOH conversion at 450 °C over  
16 studied catalysts. All spectra were collected during time-on-stream (TOS) within 0–1 h with 1

1 min interval. Band Assignments in the 40000–12500  $\text{cm}^{-1}$  are displayed in UV–vis spectra for  
2 MFI-25-M.[58, 59]

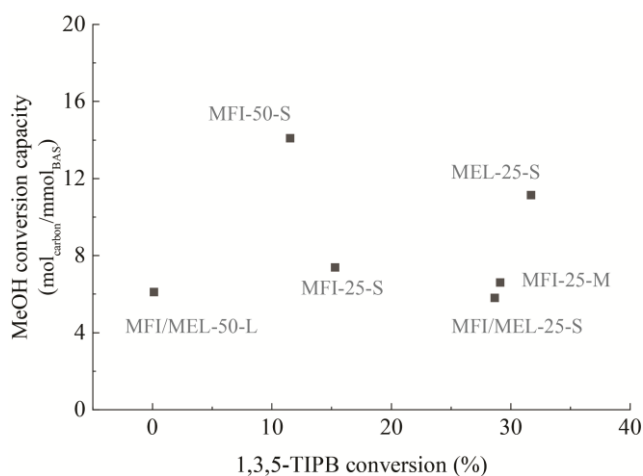
3 With operando UV–vis spectroscopy, aromatic intermediates in MTO can be determined as  
4 well as polyaromatic compounds which act as coke precursors and are thereby deactivating  
5 species.[12, 18, 58, 59, 77] Only the UV–vis spectra of the first hour of the reaction are  
6 represented as after this contributions of broad coke features are increasing in intensity (**Figure**  
7 **S8**), which results in a more difficult comparison as the individual absorbance bands are less  
8 visible. On all catalysts, three main features including the absorbance bands at ca. 35000  $\text{cm}^{-1}$ ,  
9 23000  $\text{cm}^{-1}$  and a long tail in the 20000–12000  $\text{cm}^{-1}$  are remarkable especially in the first 10  
10 spectra corresponding to TOS up to 10 min. These absorbance bands are assigned, respectively,  
11 to neutral methylated benzenes/cyclopentenyl carbocations, methylated benzene/naphthalene  
12 carbocations, and (alkylated) polyaromatics. For the MFI-type catalysts, the methylated  
13 benzenes with a characteristic absorption band at 35000  $\text{cm}^{-1}$  are widely accepted as the active  
14 species in the aromatic cycle towards the production of BTEX and ethylene [7, 12, 77, 78],  
15 whereas, the polyaromatic species giving rise to the absorbance band in the specified range  
16 20000–12000  $\text{cm}^{-1}$  are attributed to coke species [79, 80]. The shape of the UV–vis profiles  
17 along TOS differs greatly for all studied zeolites, clearly indicating the different features (e.g.,  
18 density, structure, etc.) of the retained hydrocarbons present in MTO towards the steady-state  
19 MTO product distributions. After reacting for 1 h for all zeolites, the bands at 35000  $\text{cm}^{-1}$  and  
20 23000  $\text{cm}^{-1}$  diminished in intensity while the UV–vis absorption in the broad range of 20000–  
21 12000  $\text{cm}^{-1}$  continuously grew, which is related to the accumulation of polyaromatics, probably  
22 on the external surface hindering the UV–vis absorption of inner species.[77] Compared with  
23 MFI-25-S and MFI/MEL-25-S, the relatively weak UV–vis absorption for methylated benzenes  
24 (35000  $\text{cm}^{-1}$ ) in MEL-25-S is well in line with its high propylene and low ethylene selectivity  
25 (**Figure 3**), confirming the higher contribution of the olefinic cycle in the dual-cycle mechanism.

1 Additionally, the mediated contribution of methylbenzenes for MFI/MEL-25-S is ascribed to  
2 the combination of MFI and MEL structures.

3 A faster stabilization is observed of the UV–vis absorbance bands for MFI-25-M compared  
4 to MFI-25-S . The relatively higher contribution of polyaromatics ( $20000\text{--}12000\text{ cm}^{-1}$ ) for MFI-  
5 25-M especially during the first 10 spectra might be related to its faster deactivation than MFI-  
6 25-S (**Figure 2**), and suggests blocking the access to the larger crystallites of MFI-25-M and  
7 hence a lower coke deposition (**Figure S7**). When comparing zeolites with the different Si/Al  
8 ratios, MFI-50-S shows very similar UV–vis spectra as MFI-25-S, while MFI/MEL-50-L shows  
9 a much smaller band at  $35000\text{ cm}^{-1}$ , very similar to MEL-25-S in the very early stage of the  
10 reaction. A low formation of less methylated benzenes and/or charged monoenyl/cyclopentenyl  
11 species ( $35000\text{ cm}^{-1}$ ) compared to the other zeolites, indicates a less pronounced aromatic cycle  
12 resulting in a higher propylene selectivity over MFI/MEL-50-L.

### 13 **3.4 Effect of external BAS**

14 The external acid site was characterized by the 1,3,5-TIPB cracking as a probe reaction. The  
15 critical diameter of 1,3,5-TIPB ( $> 8\text{Å}$ ) limits its diffusion into the micropores ( $< 6\text{Å}$ ) of the  
16 zeolites. Thus, the cracking of 1,3,5-TIPB selectively occurs at the external crystal surface. To  
17 investigate the effect of external acid sites on MTO stability, the 1,3,5-TIPB cracking results  
18 together with MeOH conversion capacity are plotted in **Figure 5**.



19

1 **Figure 5.** MeOH conversion capacity as a function of 1,3,5-TIPB conversion over catalysts at  
2 200 °C. Cracking conditions:  $T = 200$  °C,  $m_{\text{cat}} = 20$  mg (150–212  $\mu\text{m}$ ), 1 bar,  $P_{1,3,5\text{-TIPB}} = 0.3$   
3 kPa, carrier gas  $\text{N}_2 = 50$  mL/min. Cracking conversion was averaged within TOS=0.1–0.3h.  
4 The full picture of 1,3,5-TIPB conversion as a function of TOS were present in **Figure S9**.

5 The 1,3,5-TIPB cracking conversion indicates the different external acid site concentrations  
6 for all catalysts. Among the studied catalysts, the negligible cracking activity of MFI/MEL-50-  
7 L at 200 °C correlates with its largest crystal size (smallest external surface) and an ultimately  
8 low external acid density in comparison with MFI-50-S. The latter is also evidenced by its  
9 higher Si/Al at the external surface than MFI-50-S (**Table S2**). On the contrary, the highest  
10 1,3,5-TIPB conversion of MEL-25-S stands out and suggests the highest concentration of BAS  
11 on its external surface. XPS analysis in Figure S10 and Table S2, however, indicates a lower  
12 Al content at the external surface of MEL-25-S than that of MFI-25-M and MFI/MEL-25-S.

13 Mores *et al.* observed coke deposited on the external BAS in the MTO process blocks the  
14 pores for further access to the internal BAS, which causes the catalyst deactivation.[81]  
15 However, our results do not present a clear correlation between the concentration of the external  
16 BAS and MeOH conversion capacity (**Figure 5**). MFI/MEL-50-L showing negligible cracking  
17 activity at the outer surface also converts the lowest amount of MeOH before deactivation in  
18 the MTO test. Further, the highest MeOH conversion capacity is observed for MEL-25-S, which  
19 also shows the highest 1,3,5-TIPB cracking conversion.

### 20 **3.5 Effect of Aluminium Location**

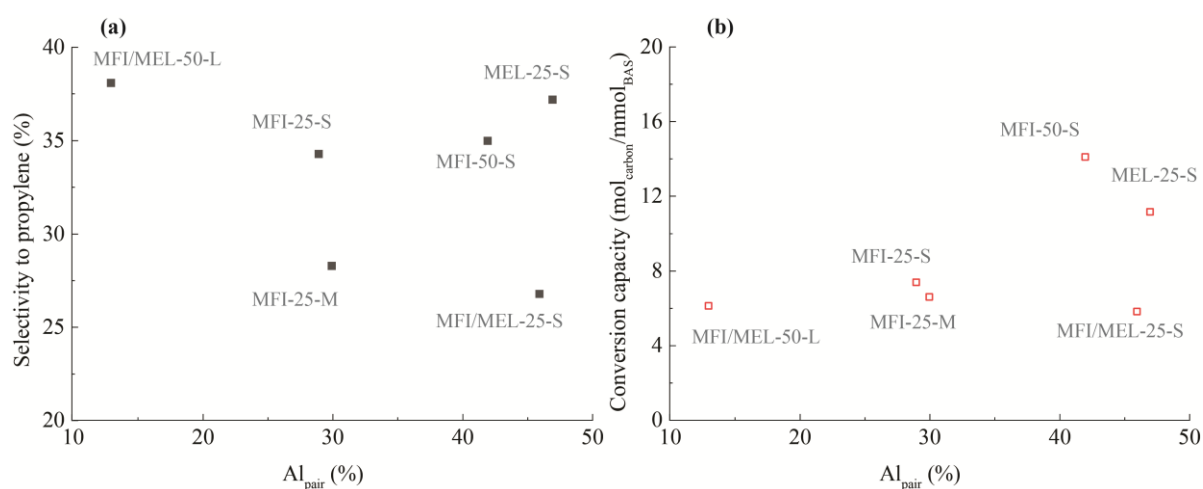
21 Recent research shows that the isomorphous substitution of T-sites by Al in the zeolite  
22 framework is not random.[82, 83] Also the BAS facing cavities or channels are associated with  
23 different catalytic activities, due to the confinement effects on the intermediates.[46, 82, 84, 85]  
24 To probe the Al distribution in the zeolite catalysts and investigate its effect on the MTO



1 performance, three techniques were applied, namely, the UV–vis analysis of Co-ion exchanged  
2 catalysts,  $^{27}\text{Al}$  MAS NMR, and C6 paraffin (3-MP and *n*-hexane) cracking tests.

### 3 3.5.1 Al Pairing

4 The Al distribution in the zeolite catalysts was first quantified by combining Co(II) ion  
5 exchange and UV–vis spectroscopy analysis. Co(II) exchange allowed quantification of Al  
6 pairing and provided an insight into the Al distribution in the framework.[49, 84] The  
7 comparison of the  $\text{Al}_{\text{pair}}$  fraction and MTO performance (regarding selectivity towards  
8 propylene and the MeOH throughput) of all zeolites is presented in **Figure 6**.



9  
10 **Figure 6.** Selectivity to propylene (a) and MeOH conversion capacity (b) versus the  
11 proportion of  $\text{Al}_{\text{pair}}$  of tested samples.  $\text{Al}_{\text{pair}}$  is measured based on Co concentration  
12 determined by ICP-AES after Co ion exchange.

13 The results in **Figure 6** and **Table S3** point to the very different Al pairing in the studied  
14 zeolites. MEL-25-S and intergrowth MFI/MEL-25-S have a large fraction of  $\text{Al}_{\text{pair}}$ , 47% and  
15 46%, respectively. Two MFI-type catalysts, MFI-25-S and MFI-25-M show a similar fraction  
16 of  $\text{Al}_{\text{pair}}$ , 29%, and 30%, respectively. MFI-50-S with the lower Al contents has 42% of  $\text{Al}_{\text{pair}}$ ,  
17 whereas MFI/MEL-50-L has only 13% of framework Al in paired configurations. The location  
18 of  $\text{Al}_{\text{pair}}$  sites was further analyzed by deconvoluting the UV–vis spectra of fully dehydrated

1 Co-exchanged samples (**Figure S11**) following the procedures reported by Dědeček *et al.*[48,  
2 49] Most of Al<sub>pair</sub> is located at the intersections, in line with the previous studies.[48, 49] MEL-  
3 25-S and intergrowth MFI/MEL-25-S have the higher fraction of Al<sub>pair</sub> (77%) at the channel  
4 intersection sites than 71–73% for MFI-25-S, MFI-25-M, and MFI-50-S. The MFI/MEL-50-L  
5 has 68% Al<sub>pair</sub> at the channel intersections.

6 Previous research indicated that Al in pair (able to host the Co<sup>2+</sup> hexa-aqua-complex during  
7 ion exchange) could cooperate during acid-catalyzed reactions such as MTO on BAS.[47] From  
8 this perspective, hydrogen transfer and aromatization reactions that require higher activation  
9 energy should occur more easily over Al<sub>pair</sub> leading to more aromatics products and lower  
10 selectivity towards propylene. However, such structure-performance correlation is not observed  
11 in this study. MEL-25-S containing the highest amount of Al<sub>pair</sub> (47%) with 77% of them at  
12 intersections shows the highest selectivity to propylene, as the typical product from the olefinic  
13 cycle in MTO process. Furthermore, results in **Figure 6(b)** suggest that the fraction of Al<sub>pair</sub>  
14 also does not correlate with the MeOH conversion capacity. MEL-25-S and MFI/MEL-25-S  
15 both contain a relatively high fraction of Al in pair compared to other catalysts. However, MEL-  
16 25-S converts the largest amount of MeOH before deactivation, whereas MFI/MEL-25-S  
17 converts the smallest amount of MeOH and represents the least stable MTO catalyst in the  
18 group of Si/Al = 25 (**Figure 2(a)**).

### 19 3.5.2 Al Location

20 NMR measurements were performed to provide a more general view of Al (no matter pairing  
21 or single) at different locations in the framework. **Figure 7** shows two dimensional (2D) <sup>27</sup>Al  
22 MQ/MAS NMR spectra with corresponding 1D <sup>27</sup>Al MAS NMR spectrum on the top in the  
23 65–45 ppm range.

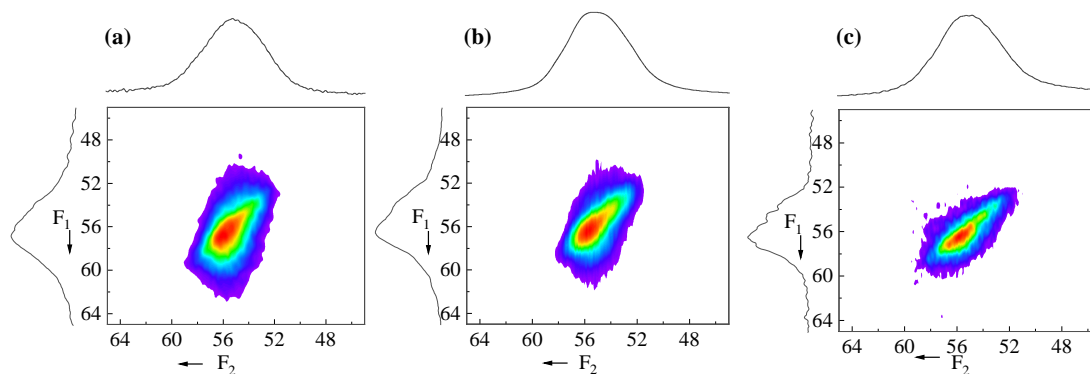


**Figure 7.** 2D  $^{27}\text{Al}$  MQ MAS NMR spectrum of (a) MEL-25-S, (b) MFI-25-M, and (c) MFI/MEL-25-S together with the isotopic projection F1 spectrum at the left and the corresponding  $^{27}\text{Al}$  MAS NMR spectrum at the top of the 2D contour profile.

All  $^{27}\text{Al}$  MAS NMR spectra contain a broad peak at 65–45 ppm and a low-intensity peak at ~0 ppm, suggesting that most Al atoms are located at tetrahedral sites (T-sites) and few Al atoms at extraframework locations with octahedral coordination.[64, 86] 2D  $^{27}\text{Al}$  MQ MAS NMR spectrum reflects the isotropic chemical shift ( $\delta_{\text{iso}}$ ) accompanied by the second-order quadrupolar effect ( $S_Q$ ) in F1 projection. The ellipsoidal 2D contour and asymmetrical F1 projection clearly show the presence of overlapping signals within 64–45 ppm, which reveals that Al is located at different T-sites in the zeolite unit cell.[83] To distinguish these Al atoms, the broad signal at 65–45 ppm were deconvoluted into five peaks at 58 ppm, 56 ppm, 55 ppm, 54 ppm and 52 ppm. The results are presented in **Figure S12** and the numerical analysis results in **Table 2**.

**Table 2.** The fraction of various peaks obtained from the  $^{27}\text{Al}$  MAS NMR spectrum.

	$\text{Al}_{\text{intersection}} / \%$	$\text{Al}_{\text{channel}} / \%$	Characteristic peaks proportion / %				
			$58 \pm 0.3$ ppm	$56 \pm 0.2$ ppm	$55 \pm 0.5$ ppm	$53 \pm 0.4$ ppm	$52 \pm 0.3$ ppm
MEL-25-S	46.4	53.6	11.1	24.0	29.6	24.1	11.2
MFI-25-S	47.9	52.1	9.0	28.6	24.2	23.6	14.7
MFI/MEL-25-S	48.7*	51.3*	14.2	25.0	28.6	24.1	8.2
MFI-25-M	49.3	50.7	11.7	25.5	24.8	25.3	12.7
MFI-50-S	47.0	53.0	8.0	26.9	25.5	26.1	13.5
MFI/MEL-50-L	45.2*	54.8*	15.3	32.1	31.8	18.3	2.5

\*: Al proportions for intergrowth samples were calculated based on the fraction of MFI and MEL phase in **Table S1**.

1

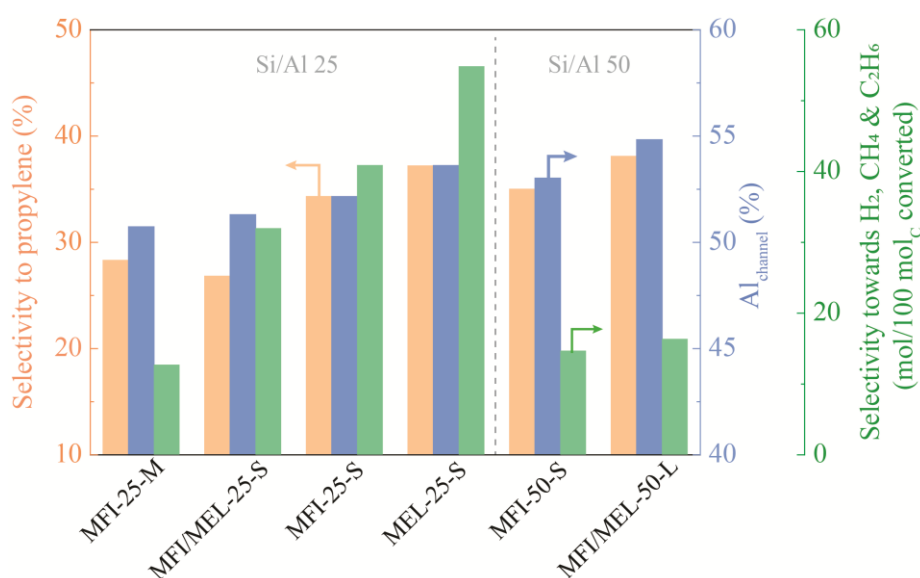
2       Significantly different proportions of the characteristic peaks were obtained for all zeolites  
3 (**Table 2**), which indicate the diverging Al distribution over the different positions in the  
4 frameworks.

5       Based on the combination of the C6 paraffin cracking and  $^{27}\text{Al}$  MAS NMR deconvolution  
6 results, Yokoi et al. attributed the peak at 56 ppm and 53 to the T-sites facing the straight or  
7 sinusoidal channels, whereas the signal at 54-55 ppm was assigned to the T-sites of ZSM-5  
8 intersections.[42] A similar assignment for ZSM-11 zeolite was carried on the basis of DFT  
9 calculations by Wang et al [33]. Here, the peaks at 56 ppm and 55 ppm were assigned to T-sites  
10 facing the straight channels, while the other peaks in the  $^{27}\text{Al}$  MAS NMR spectra to the  
11 intersection sites of ZSM-11. Following these assignments, our data (**Table 2**) reveal that in the  
12 group with Si/Al 25, MEL-25-S contains the highest fraction of Al in the straight channels. The  
13 related MFI-25-S shows a comparable Al distribution with only a slightly higher fraction of Al  
14 occupying the intersection sites. The preference for Al sitting at the intersection sites is most  
15 pronounced for MFI/MEL-25-S and MFI-25-M samples. At lower Al content, the fraction of  
16 Al in the channels slightly increases suggesting a better Al dispersion in the lattice.

17       The results in **Table 2** suggest that the  $\text{Al}_{\text{channel}}$  fraction and selectivity to propylene and  
18 butylene (**Figure 3** and **S6**) correlate well for all studied catalysts. MEL-25-S and MFI/MEL-  
19 50-L show the highest selectivities of propylene (35–36%) and butylenes (16-18%) in line with  
20 their highest fraction of Al in the channels. However, in view of the typical  $\pm 5\%$  uncertainty in  
21 the deconvolution of  $^{27}\text{Al}$  MAS NMR spectra [87], additional characterization of the Al  
22 distribution was carried out.

23       To further distinguish framework Al located in channels or intersections, 3-methylpentane  
24 (3-MP) cracking at 400 °C was performed on all catalysts. The location of framework Al was

1 based on the different product selectivity observed, originating from the different transition-  
2 state shape selectivity for intersection or channel. Monomolecular 3-MP cracking selectively  
3 forms hydrogen, methane, and ethane, whereas the simultaneous bimolecular cracking forms  
4 larger carbenium ions and eventually aromatics via the classical hydrogen transfer and  
5 dehydrogenation reactions and hardly yields products below C<sub>3</sub>.(Scheme S1) Because  
6 bimolecular cracking via a bulky transition state is more restricted than monomolecular  
7 cracking in the narrow channels of ZSM-5 or ZSM-11, the production level of lower  
8 hydrocarbons (methane and ethane) and hydrogen from monomolecular cracking can be used  
9 to describe the proportion of Al in the channels.[42, 88] 2,4-DMQ was added to avoid  
10 unselective cracking at the external crystallite surface.



11  
12 **Figure 8.** Carbon selectivity to propylene versus selectivity towards hydrogen, methane and  
13 ethane of 3-MP monomolecular cracking over samples with Si/Al of 25 (a) and Si/Al of 50  
14 (b). 3-MP cracking conditions:  $T = 400$  °C,  $m_{\text{cat}} = 20$  mg (150–212  $\mu\text{m}$ ), 1 bar, carrier gas  $\text{N}_2$   
15 = 50 mL/min, 3-MP partial pressure = 3.8 kPa in the presence of 2,4-DMQ (<0.1 kPa). The  
16 product selectivity is averaged values within TOS = 0.1–0.4 h. The full-scale picture along  
17 TOS is given in **Figure S13**.

1 The shape selectivity of different zeolite topologies for *n*-hexane and 3-MP cracking has  
2 also been quantified by the so-called constraint index (CI) presented in section 2.3.[42, 89, 90]  
3 In our case, however, the studied materials possess a very similar channel/intersection structure  
4 and the sensitivity of this approach becomes less distinctive. Furthermore, the heterogeneous  
5 position distribution of lattice Al, shown by <sup>27</sup>Al MAS NMR, will affect the cracking  
6 mechanism of 3-MP leading to different 3-MP conversions and CI values.[42] As example  
7 serves the CI test over MFI-25-S and MEL-25-S here. The *n*-hexane and 3-MP cracking  
8 (**Figure S14**) over MEL-25-S and MFI-25-S shows that the CI (constraint index) value for  
9 MEL-25-S (1.2) is slightly larger than for MFI-25-S (1.0), and would suggest a larger steric  
10 hindrance in MEL-25-S than MFI-25-S.[42, 89, 90] However, this observation is opposite to  
11 the fact that the pore size of MEL is slightly larger than MFI. Thus, in this study, CI serves  
12 more as a descriptor for a different lattice Al-distribution rather than a steric reactant hindrance  
13 of zeolite topology [42].

14 The overall 3-MP conversion of <5% for all materials is well located in the differential  
15 regime, so activity and product selectivity can be directly compared.[91] Accordingly, an  
16 excellent correlation between MTO selectivity to propylene and 3-MP cracking selectivity  
17 towards hydrogen, methane and ethane is observed for samples with the same Al content (Si/Al  
18 = 25 or 50). MEL-25-S shows the highest selectivity towards hydrogen, methane and ethane  
19 (55%), whereas MFI-25-M the lowest selectivity (13%). Combined with **Table 2**, this means  
20 that the higher the fraction of Al in channels, the higher the selectivity towards propylene in  
21 MTO regardless of the zeolite structure except for MFI/MEL-25-S. Interestingly, an even better  
22 correlation between selectivity to propylene and Al fraction at channels is observed when the  
23 selectivity at steady-state conditions (MeOH conversion of 100% at TOS of 1 h in **Figure S5**)  
24 is chosen for all catalysts, in which MFI/MEL-25-S exhibits a higher selectivity to propylene  
25 than MFI-25-M.

1        These results correlate well with the deconvolution results from  $^{27}\text{Al}$  MAS NMR, which  
2 also indicates a higher fraction of Al in the channels on MEL-25-S than on MFI-25-M. An  
3 indicative trend between MTO propylene selectivity (activity of olefinic cycle) and Al location  
4 in the channel from NMR and from 3-MP cracking is also found for the samples with Si/Al of  
5 50. With the lower Al content of MFI-50-S and MFI/MEL-50-L, the bimolecular cracking of  
6 3-MP is a more dominant pathway because of the much lower activation energy [54], resulting  
7 in selectivity towards methane, ethane and hydrogen below 17%. This also accounts for the  
8 higher total 3-MP conversion data (**Table S4**) for the samples (Si/Al = 25) with a higher Al  
9 fraction in the intersections (**Table 2**). The exceptional case is MFI-50-S. It exhibits the second  
10 highest 3-MP conversion of 3.3% among all studied materials, which might indicate the  
11 extraordinarily high proportion of Al located at the intersection and the lower selectivity to  
12 propylene than MFI/MEL-50-L.

### 13        **3.6 Discussion**

14        The objective of this study was to reveal key performance parameters of three 10-MR zeolite  
15 catalysts, *viz.* MFI, MEL, and a mixed MFI/MEL structure, in the MTO reaction, with the focus  
16 on MTO activity, product selectivity (propylene) and stability for two Si/Al ratios. MEL has a  
17 similar channel/intersection system as MFI with similar (slightly larger) nano-scale dimensions,  
18 but with only straight channels, while MFI/MEL samples contain an MFI and MEL intergrowth  
19 structure, which is more than simply a physical mixture.

20        MTO tests and *operando* UV–vis spectroscopy measurements reveal completely different  
21 product distributions and MTO lifetimes coupled with the different features of retained  
22 hydrocarbons in all three zeolite structures. With the same Al content (origin of the BAS) and  
23 BAS strength, the MEL-type zeolite is shown as the most propylene-selective catalyst in the  
24 MTO test, which is in line with reported observations.[33, 92] Unlike the shorter MTO lifetime  
25 of MEL-type zeolites than of MFI-type zeolites in [33], in our study MEL-25-S exhibits the

1 highest MeOH conversion capacity, more than 50% higher than MFI-25-S and MFI/MEL-25-  
2 S. On the other hand, MFI/MEL-50-L shows the higher selectivity to propylene than MFI-50-  
3 S. Even two MFI-type samples with Si/Al of 25 exhibit different MTO performance regarding  
4 conversion capacity and product selectivity. All these observations indicate that besides the  
5 zeolite topology and Al content (BAS density) other parameters are involved in controlling their  
6 catalytic performance.

7 Of the various techniques applied only the 3-MP cracking, and the  $^{27}\text{Al}$  MAS NMR spectra  
8 analysis revealed a clear correlation between the propylene selectivity in MTO with the Al  
9 located in the channels of the zeolites, regardless of zeolite framework and crystal size (**Figure**  
10 **8**): the more Al located in the channels, the higher the selectivity to propylene and butylenes is  
11 observed. This seems the primary key performance parameter in this reaction. This suggests  
12 that 1D 10-MR zeolites, containing only channels would be the preferred catalysts, completely  
13 suppressing the aromatics-based cycle. Indeed, no aromatic products were observed for ZSM-  
14 22 and ZSM-23 catalysts, although ZSM-48 with slightly wider channels did.[73, 93]  
15 Aromatics were formed in all catalysts, but were trapped in the former systems and only could  
16 diffuse out of the latter, similarly as for 1D 12-MR ZSM-12 [94]. Comparing ZSM-22 with  
17 ZSM-5 and ZSM-11 revealed, however, a lower propylene selectivity, ~38% versus ~50%, and  
18 a much shorter lifetime [26]. Introduction of mesoporosity by desilication and acid treatment  
19 doubled the ZSM-22 lifetime with retained shape selectivity [33], suggesting an easier escape  
20 of coke precursors like in the case of ZSM-48 [73]. So, the high propylene and butylene  
21 selectivity of the 10-MR MEL-25-S is attributed to its high fraction of Al located in the channels,  
22 similar as for the mixed phase MFI/MEL-50-L. The latter has the highest light olefin selectivity,  
23 indicating that an optimal BAS concentration exists for an optimal performance [31]. Our  
24 results confirm the results of Wang *et al.*[33] observing and Al enrichment in the intersections  
25 of ZSM-5 and in the channels of ZSM-11. We further extend this rule to the intergrowth



1 MFI/MEL samples. These findings provide a rational basis for the targeted synthesis of 3D 10-  
2 MR zeolites with only Al located in the channels for improved olefin production. An  
3 enrichment of Al in the channels was indeed obtained by Li et al.[82] by preparation of B-Al-  
4 ZSM-5 and removal of B that preferentially resided in the intersections. This indeed improved  
5 the propylene and butylene selectivity in MTO. These post-synthesis approaches confirm the  
6 attempts to concentrate Al in the channels of ZSM-5 (or remove it from the intersections) to  
7 improve the MeOH selectivity towards the lower olefins, in agreement with the results for  
8 theta-1 (TON-type, 1D zeolite) [34, 95].

9 The correlation between Al located in the channels and MeOH selectivity towards propylene  
10 (or light olefins) holds for all three zeolite structures, which further suggests the Al location is  
11 a more significant factor than zeolite structure, at least among MFI, MEL, and MFI/MEL in  
12 MTO, while other properties (crystal size, Al-content and external BAS) are of secondary  
13 influence (less pronounced), affecting selectivity, coke deposition, and time-on-stream MTO  
14 activity.

15 It is rather difficult to determine a single key parameter controlling the MTO deactivation  
16 in this study. Smaller crystals provide shorter diffusion distances for (poly)aromatics to escape  
17 and a larger external area (capacity) for coke deposition. In larger crystals, the lower coke  
18 deposition in the outer crystal regions can limit accessibility to the BAS resulting in a faster  
19 deactivation and less coke. This might also explain the fast deactivation for MFI-25-M in  
20 comparison with other catalysts with the smaller crystal size.

21 Co(II) ion-exchange coupled with *ex-situ* UV-vis analysis reveals that a large fraction of  
22  $Al_{pair}$  is located in the intersection regardless of Si/Al and zeolite structure. But there is no clear  
23 correlation between  $Al_{pair}$  information (fraction or location) with the MTO deactivation. Both  
24 MEL and MFI/MEL catalysts with the same Al content contain ca. 46%  $Al_{pair}$  with more than  
25 70% of them in the intersection, but the MEL-type zeolite is shown as the most stable, while

1 MFI/MEL-25-S the least stable catalyst in the MTO test (**Figure 2**). Another notorious example  
2 is MFI/MEL-50-L, which contains the smallest fraction of Al<sub>pair</sub> but deactivates quickly in MTO.  
3 By applying 1,3,5-TIPB cracking, probing the acidity on the external surface of the samples,  
4 combined with XPS analysis (**Table S2**), a heterogeneous distribution of Al within the zeolite  
5 particle is observed. As the uncontrolled alkylation of hydrocarbons leading to coke deposition  
6 on the external BAS in MTO could block the pores for further access to the internal active sites  
7 [81], a less acidic outer surface expectedly correlates with the longer MTO lifetime and vice-  
8 versa. It explains the exceptionally high level of external BAS coupled with the low MeOH  
9 conversion capacity on MFI-25-M (**Figure 5**). The intergrowth sample with Si/Al of 25 shows  
10 the highest level of external BAS, corresponding with the lowest MeOH conversion capacity  
11 (**Figure 5**) in comparison with the MFI-type and MEL-type samples with the same Al content  
12 and crystal size. However, MEL-25-S exceptionally contains a higher fraction of external BAS  
13 but shows a higher MeOH conversion capacity than MFI-25-S, while MFI/MEL-50-L shows  
14 negligible external BAS coupled with a much lower MeOH conversion capacity than MFI-50-  
15 S. Clearly, the impact of Al distribution in the framework cannot be ignored. The MTO  
16 deactivation is closely related to the activity of the aromatic-based cycle, as polyaromatics are  
17 commonly described as the coke species. The higher level of Al located in the channels not  
18 only directs the MeOH selectivity towards light olefins, but also reduces the contribution of the  
19 competing aromatic-based cycle eventually leading to polyaromatics deposition. This might  
20 explain the high production of light olefins coupled with the largest MeOH conversion capacity  
21 for the MEL-type catalyst.

## 22 **4. Conclusions**

23 The property-performance relationship in the MTO process for three zeolite structures of  
24 MFI, MEL, and intergrowth MFI/MEL were evaluated via a series of characterization  
25 techniques and probe reactions. The MTO test combined with *operando* UV–vis spectroscopy

1 shows that product selectivity, MeOH conversion capacity, and retained hydrocarbons before  
2 deactivation are significantly different for the studied zeolites. Besides the morphology and Al  
3 content, more intrinsic aspects concerning Al distribution were revealed and their correlations  
4 with the catalytic performance were discussed. Through  $^{27}\text{Al}$  MAS NMR analysis and 3-MP  
5 cracking, an excellent correlation between Al location and MeOH selectivity towards propylene  
6 and butylenes is observed regardless of the different zeolite frameworks. The higher level of Al  
7 located in the channels (straight or sinusoidal) suppresses the propagation of the aromatic cycle,  
8 which requires spacious space like intersections, and favours the olefinic cycle. Therefore, the  
9 MeOH selectivity towards  $\text{C}_3\text{-C}_4$  light olefins is considerably improved for MEL-type and one  
10 MFI/MEL intergrowth zeolite containing the highest fraction of Al in the channels. The  
11 intergrowth of MFI and MEL phases accelerates the catalyst deactivation rate evidenced by the  
12 lowest MeOH conversion capacities in the MTO process.

13 Other zeolite parameters as  $\text{Al}_{\text{pair}}$  and external BAS concentration, evaluated via Co ion-  
14 exchange technique and 1,3,5-TIPB cracking, showed lack of a clear correlation with MeOH  
15 selectivity and suggests these parameters are of less pronounced influence on product  
16 distribution, specifically the production of propylene. No correlation between these parameters  
17 and MeOH conversion capacity was obtained, revealing MTO deactivation is a rather complex  
18 process, which cannot be captured by a single parameter. Crystal size, Al-content, external BAS  
19 and Al-distribution in the framework all affect the deactivation. All these characterizations and  
20 probe reactions still comprise part of catalyst properties that potentially affect the catalytic  
21 performance. More key parameters, such as diffusivity within the zeolite micropore [96] are  
22 not analysed quantitatively in this study, but their impact on the MTO mechanism especially  
23 for the intergrowth MFI/MEL samples cannot be ignored.

24 This work not only provides the direct relationship between zeolite acidic properties and  
25 their catalytic influence in the MTO process benefiting the rational catalyst design for the MTO

1 process but also reveals that methanol transformation in the zeolite is an extremely complex  
2 process, which is affected by multiple parameters to a different level. Our study also highlights  
3 the importance of an integrated approach to characterize and analyse all intrinsic properties of  
4 zeolite catalysts in the MTO process.

## 5 **5. Acknowledgment**

6 We acknowledge BASF and the Advanced Research Center Chemical Building Blocks  
7 Consortium (ARC CBBC) for funding under project number 2016.007.TUD.

## 6. References

1. Olah, G.A., *Beyond Oil and Gas: The Methanol Economy*. Angewandte Chemie International Edition, 2005. **44**(18): p. 2636-2639.
2. Olah, G.A., A. Goepfert, and G.S. Prakash, *Chemical recycling of carbon dioxide to methanol and dimethyl ether: from greenhouse gas to renewable, environmentally carbon neutral fuels and synthetic hydrocarbons*. The Journal of Organic Chemistry, 2008. **74**(2): p. 487-498.
3. Mota, F.M. and D.H. Kim, *From CO<sub>2</sub> methanation to ambitious long-chain hydrocarbons: alternative fuels paving the path to sustainability*. Chemical Society Reviews, 2019. **48**(1): p. 205-259.
4. Keil, F.J., *Methanol-to-hydrocarbons: process technology*. Microporous and Mesoporous Materials, 1999. **29**(1): p. 49-66.
5. Tian, P., Y. Wei, M. Ye, and Z. Liu, *Methanol to Olefins (MTO): From Fundamentals to Commercialization*. ACS Catalysis, 2015. **5**(3): p. 1922-1938.
6. Xie, Z., J. Liu, S. Zhong, and H. Zhang, *Process for producing light olefins from methanol or dimethyl ether*, U.S.P.a.T. Office, Editor. 2014, China Petroleum and Chemical Corp Sinopec Shanghai Research Institute of Petrochemical Technology.
7. Svelle, S., F. Joensen, J. Nerlov, U. Olsbye, K.-P. Lillerud, S. Kolboe, and M. Bjørgen, *Conversion of Methanol into Hydrocarbons over Zeolite H-ZSM-5: Ethene Formation Is Mechanistically Separated from the Formation of Higher Alkenes*. Journal of the American Chemical Society, 2006. **128**(46): p. 14770-14771.
8. Xu, S., A. Zheng, Y. Wei, J. Chen, J. Li, Y. Chu, M. Zhang, Q. Wang, Y. Zhou, J. Wang, F. Deng, and Z. Liu, *Direct Observation of Cyclic Carbenium Ions and Their Role in the Catalytic Cycle of the Methanol-to-Olefin Reaction over Chabazite Zeolites*. Angewandte Chemie International Edition, 2013. **52**(44): p. 11564-11568.
9. Olsbye, U., S. Svelle, K. Lillerud, Z. Wei, Y. Chen, J. Li, J. Wang, and W. Fan, *The formation and degradation of active species during methanol conversion over protonated zeotype catalysts*. Chemical Society Reviews, 2015. **44**(20): p. 7155-7176.
10. Wu, X., S. Xu, W. Zhang, J. Huang, J. Li, B. Yu, Y. Wei, and Z. Liu, *Direct Mechanism of the First Carbon-Carbon Bond Formation in the Methanol-to-Hydrocarbons Process*. Angewandte Chemie International Edition, 2017. **56**(31): p. 9039-9043.
11. Li, C., C. Paris, J. Martínez-Triguero, M. Boronat, M. Moliner, and A. Corma, *Synthesis of reaction-adapted zeolites as methanol-to-olefins catalysts with mimics of reaction intermediates as organic structure-directing agents*. Nature Catalysis, 2018. **1**(7): p. 547-554.
12. Yarulina, I., K. De Wispelaere, S. Bailleul, J. Goetze, M. Radersma, E. Abou-Hamad, I. Vollmer, M. Goesten, B. Mezari, E.J.M. Hensen, J.S. Martínez-Espín, M. Morten, S. Mitchell, J. Perez-Ramirez, U. Olsbye, B.M. Weckhuysen, V. Van Speybroeck, F. Kapteijn, and J. Gascon, *Structure-performance descriptors and the role of Lewis acidity in the methanol-to-propylene process*. Nature Chemistry, 2018. **10**(8): p. 804-812.
13. McCann, D.M., D. Lesthaeghe, P.W. Kletnieks, D.R. Guenther, M.J. Hayman, V. Van Speybroeck, M. Waroquier, and J.F. Haw, *A complete catalytic cycle for supramolecular methanol-to-olefins conversion by linking theory with experiment*. Angewandte Chemie International Edition, 2008. **47**(28): p. 5179-5182.
14. Ilias, S. and A. Bhan, *Tuning the selectivity of methanol-to-hydrocarbons conversion on H-ZSM-5 by co-processing olefin or aromatic compounds*. Journal of Catalysis, 2012. **290**: p. 186-192.
15. Hwang, A. and A. Bhan, *Deactivation of Zeolites and Zeotypes in Methanol-to-Hydrocarbons Catalysis: Mechanisms and Circumvention*. Accounts of Chemical Research, 2019. **52**(9): p. 2647-2656.
16. Yarulina, I., A.D. Chowdhury, F. Meirer, B.M. Weckhuysen, and J. Gascon, *Recent trends and fundamental insights in the methanol-to-hydrocarbons process*. Nature Catalysis, 2018. **1**(6): p. 398-411.
17. Stöcker, M., *Methanol-to-hydrocarbons: catalytic materials and their behavior* Dedicated to my wife Wencke Ophaug.1. Microporous and Mesoporous Materials, 1999. **29**(1): p. 3-48.

- 1 18. Olsbye, U., S. Svelle, M. Bjørgen, P. Beato, T.V.W. Janssens, F. Joensen, S. Bordiga, and K.P.  
2 Lillerud, *Conversion of Methanol to Hydrocarbons: How Zeolite Cavity and Pore Size Controls Product*  
3 *Selectivity*. *Angewandte Chemie International Edition*, 2012. **51**(24): p. 5810-5831.
- 4 19. Ilias, S. and A. Bhan, *Mechanism of the Catalytic Conversion of Methanol to Hydrocarbons*. *ACS*  
5 *Catalysis*, 2013. **3**(1): p. 18-31.
- 6 20. Bjørgen, M., U. Olsbye, D. Petersen, and S. Kolboe, *The methanol-to-hydrocarbons reaction:*  
7 *insight into the reaction mechanism from [<sup>12</sup>C] benzene and [<sup>13</sup>C] methanol coreactions over zeolite H-*  
8 *beta*. *Journal of Catalysis*, 2004. **221**(1): p. 1-10.
- 9 21. Song, W., H. Fu, and J.F. Haw, *Supramolecular origins of product selectivity for methanol-to-*  
10 *olefin catalysis on HSAPO-34*. *Journal of the American Chemical Society*, 2001. **123**(20): p. 4749-4754.
- 11 22. Olsbye, U., S. Svelle, M. Bjørgen, P. Beato, T.V. Janssens, F. Joensen, S. Bordiga, and K.P. Lillerud,  
12 *Conversion of methanol to hydrocarbons: how zeolite cavity and pore size controls product selectivity*.  
13 *Angewandte Chemie International Edition*, 2012. **51**(24): p. 5810-5831.
- 14 23. Svelle, S., F. Joensen, J. Nerlov, U. Olsbye, K.-P. Lillerud, S. Kolboe, and M. Bjørgen, *Conversion*  
15 *of methanol into hydrocarbons over zeolite H-ZSM-5: Ethene formation is mechanistically separated*  
16 *from the formation of higher alkenes*. *Journal of the American Chemical Society*, 2006. **128**(46): p.  
17 14770-14771.
- 18 24. Ilias, S., R. Khare, A. Malek, and A. Bhan, *A descriptor for the relative propagation of the*  
19 *aromatic-and olefin-based cycles in methanol-to-hydrocarbons conversion on H-ZSM-5*. *Journal of*  
20 *Catalysis*, 2013. **303**: p. 135-140.
- 21 25. Khare, R., Z. Liu, Y. Han, and A. Bhan, *A mechanistic basis for the effect of aluminum content*  
22 *on ethene selectivity in methanol-to-hydrocarbons conversion on HZSM-5*. *Journal of Catalysis*, 2017.  
23 **348**: p. 300-305.
- 24 26. Wei, R., C. Li, C. Yang, and H. Shan, *Effects of ammonium exchange and Si/Al ratio on the*  
25 *conversion of methanol to propylene over a novel and large partical size ZSM-5*. *Journal of Natural Gas*  
26 *Chemistry*, 2011. **20**(3): p. 261-265.
- 27 27. Danilina, N., F. Krumeich, S.A. Castelanelli, and J.A. van Bokhoven, *Where are the active sites*  
28 *in zeolites? Origin of aluminum zoning in ZSM-5*. *The Journal of Physical Chemistry C*, 2010. **114**(14): p.  
29 6640-6645.
- 30 28. Pashkova, V., S. Sklenak, P. Klein, M. Urbanova, and J. Dědeček, *Location of Framework Al*  
31 *Atoms in the Channels of ZSM-5: Effect of the (Hydrothermal) Synthesis*. *Chemistry – A European*  
32 *Journal*, 2016. **22**(12): p. 3937-3941.
- 33 29. Smit, B. and T.L. Maesen, *Towards a molecular understanding of shape selectivity*. *Nature*, 2008.  
34 **451**(7179): p. 671-678.
- 35 30. Hereijgers, B.P., F. Bleken, M.H. Nilsen, S. Svelle, K.-P. Lillerud, M. Bjørgen, B.M. Weckhuysen,  
36 and U. Olsbye, *Product shape selectivity dominates the Methanol-to-Olefins (MTO) reaction over H-*  
37 *SAPO-34 catalysts*. *Journal of Catalysis*, 2009. **264**(1): p. 77-87.
- 38 31. Dyballa, M., P. Becker, D. Trefz, E. Klemm, A. Fischer, H. Jakob, and M. Hunger, *Parameters*  
39 *influencing the selectivity to propene in the MTO conversion on 10-ring zeolites: directly synthesized*  
40 *zeolites ZSM-5, ZSM-11, and ZSM-22*. *Applied Catalysis A: General*, 2016. **510**: p. 233-243.
- 41 32. Yu, Q., C. Cui, Q. Zhang, J. Chen, Y. Li, J. Sun, C. Li, Q. Cui, C. Yang, and H. Shan, *Hierarchical*  
42 *ZSM-11 with intergrowth structures: Synthesis, characterization and catalytic properties*. *Journal of*  
43 *Energy Chemistry*, 2013. **22**(5): p. 761-768.
- 44 33. Wang, S., P. Wang, Z. Qin, Y. Chen, M. Dong, J. Li, K. Zhang, P. Liu, J. Wang, and W. Fan, *Relation*  
45 *of Catalytic Performance to the Aluminum Siting of Acidic Zeolites in the Conversion of Methanol to*  
46 *Olefins, Viewed via a Comparison between ZSM-5 and ZSM-11*. *ACS Catalysis*, 2018. **8**(6): p. 5485-5505.
- 47 34. Dyballa, M., U. Obenaus, M. Rosenberger, A. Fischer, H. Jakob, E. Klemm, and M. Hunger, *Post-*  
48 *synthetic improvement of H-ZSM-22 zeolites for the methanol-to-olefin conversion*. *Microporous and*  
49 *Mesoporous Materials*, 2016. **233**: p. 26-30.
- 50 35. Teketel, S., U. Olsbye, K.P. Lillerud, P. Beato, and S. Svelle, *Co-conversion of methanol and light*  
51 *alkenes over acidic zeolite catalyst H-ZSM-22: Simulated recycle of non-gasoline range products*.  
52 *Applied Catalysis A: General*, 2015. **494**: p. 68-76.

- 1 36. Wang, J., Y. Wei, J. Li, S. Xu, W. Zhang, Y. He, J. Chen, M. Zhang, A. Zheng, and F. Deng, *Direct*  
2 *observation of methylcyclopentenyl cations (MCP+) and olefin generation in methanol conversion over*  
3 *TON zeolite*. *Catalysis Science & Technology*, 2016. **6**(1): p. 89-97.
- 4 37. Baerlocher, C. and L. McCusker, *Database of Zeolite Structures, 2008*. [http://www.iza-](http://www.iza-structure.org/databases)  
5 [structure.org/databases](http://www.iza-structure.org/databases), 2019.
- 6 38. Millward, G.R., S. Ramdas, J.M. Thomas, and M.T. Barlow, *Evidence for semi-regularly ordered*  
7 *sequences of mirror and inversion symmetry planes in ZSM-5/ZSM-11 shape-selective zeolitic catalysts*.  
8 *Journal of the Chemical Society, Faraday Transactions 2: Molecular and Chemical Physics*, 1983. **79**(7):  
9 p. 1075-1082.
- 10 39. Conte, M., B. Xu, T.E. Davies, J.K. Bartley, A.F. Carley, S.H. Taylor, K. Khalid, and G.J. Hutchings,  
11 *Enhanced selectivity to propene in the methanol to hydrocarbons reaction by use of ZSM-5/11*  
12 *intergrowth zeolite*. *Microporous and Mesoporous Materials*, 2012. **164**: p. 207-213.
- 13 40. Zhong, J., J. Han, Y. Wei, and Z. Liu, *Catalysts and shape selective catalysis in the methanol-to-*  
14 *olefin (MTO) reaction*. *Journal of Catalysis*, 2021. **396**: p. 23-31.
- 15 41. Emeis, C., *Determination of integrated molar extinction coefficients for infrared absorption*  
16 *bands of pyridine adsorbed on solid acid catalysts*. *Journal of Catalysis*, 1993. **141**(2): p. 347-354.
- 17 42. Yokoi, T., H. Mochizuki, S. Namba, J.N. Kondo, and T. Tatsumi, *Control of the Al Distribution in*  
18 *the Framework of ZSM-5 Zeolite and Its Evaluation by Solid-State NMR Technique and Catalytic*  
19 *Properties*. *The Journal of Physical Chemistry C*, 2015. **119**(27): p. 15303-15315.
- 20 43. Petrakis, L., *Spectral line shapes: Gaussian and Lorentzian functions in magnetic resonance*.  
21 *Journal of Chemical Education*, 1967. **44**(8): p. 432.
- 22 44. Chen, K., *A Practical Review of NMR Lineshapes for Spin-1/2 and Quadrupolar Nuclei in*  
23 *Disordered Materials*. *International Journal of Molecular Sciences*, 2020. **21**(16): p. 5666.
- 24 45. Holzinger, J., P. Beato, L.F. Lundegaard, and J. Skibsted, *Distribution of Aluminum over the*  
25 *Tetrahedral Sites in ZSM-5 Zeolites and Their Evolution after Steam Treatment*. *The Journal of Physical*  
26 *Chemistry C*, 2018. **122**(27): p. 15595-15613.
- 27 46. Liang, T., J. Chen, Z. Qin, J. Li, P. Wang, S. Wang, G. Wang, M. Dong, W. Fan, and J. Wang,  
28 *Conversion of methanol to olefins over H-ZSM-5 zeolite: Reaction pathway is related to the framework*  
29 *aluminum siting*. *ACS Catalysis*, 2016. **6**(11): p. 7311-7325.
- 30 47. Dědeček, J., E. Tabor, and S. Sklenak, *Tuning the Aluminum Distribution in Zeolites to Increase*  
31 *their Performance in Acid-Catalyzed Reactions*. *ChemSusChem*, 2019. **12**(3): p. 556-576.
- 32 48. Dědeček, J., D. Kaucký, and B. Wichterlová, *Co<sup>2+</sup> ion siting in pentasil-containing zeolites, part*  
33 *3.: Co<sup>2+</sup> ion sites and their occupation in ZSM-5: a VIS diffuse reflectance spectroscopy study*.  
34 *Microporous and Mesoporous Materials*, 2000. **35-36**: p. 483-494.
- 35 49. Dědeček, J., D. Kaucký, B. Wichterlová, and O. Gonsiorová, *Co<sup>2+</sup> ions as probes of Al distribution*  
36 *in the framework of zeolites. ZSM-5 study*. *Physical Chemistry Chemical Physics*, 2002. **4**(21): p. 5406-  
37 5413.
- 38 50. Verberckmoes, A.A., B.M. Weckhuysen, and R.A. Schoonheydt, *Spectroscopy and coordination*  
39 *chemistry of cobalt in molecular sieves*. *Microporous and Mesoporous Materials*, 1998. **22**(1-3): p. 165-  
40 178.
- 41 51. Tabor, E., M. Bernauer, B. Wichterlova, and J. Dedecek, *Enhancement of propene*  
42 *oligomerization and aromatization by proximate protons in zeolites. FTIR study of the reaction pathway*  
43 *in ZSM-5*. *Catalysis Science & Technology*, 2019.
- 44 52. Namba, S., S. Nakanishi, and T. Yashima, *Behavior of quinoline derivatives as poisons in*  
45 *isomerization of p-xylene on HZSM-5 zeolite*. *Journal of Catalysis*, 1984. **88**(2): p. 505-508.
- 46 53. Namba, S., A. Inaka, and T. Yashima, *Effect of selective removal of aluminium from external*  
47 *surfaces of HZSM-5 zeolite on shape selectivity*. *Zeolites*, 1986. **6**(2): p. 107-110.
- 48 54. Krannila, H., W.O. Haag, and B.C. Gates, *Monomolecular and bimolecular mechanisms of*  
49 *paraffin cracking: n-butane cracking catalyzed by HZSM-5*. *Journal of Catalysis*, 1992. **135**(1): p. 115-  
50 124.
- 51 55. Haag, W.O., R.M. Lago, and P.B. Weisz, *Transport and reactivity of hydrocarbon molecules in a*  
52 *shape-selective zeolite*. *Faraday Discussions of the Chemical Society*, 1981. **72**: p. 317-330.

- 1 56. Frillette, V.J., W.O. Haag, and R.M. Lago, *Catalysis by crystalline aluminosilicates: Characterization of intermediate pore-size zeolites by the "Constraint Index"*. Journal of Catalysis, 1981.  
2 **67**(1): p. 218-222.
- 3  
4 57. Janssens, T.V.W., *A new approach to the modeling of deactivation in the conversion of*  
5 *methanol on zeolite catalysts*. Journal of Catalysis, 2009. **264**(2): p. 130-137.
- 6 58. Goetze, J., F. Meirer, I. Yarulina, J. Gascon, F. Kapteijn, J. Ruiz-Martínez, and B.M. Weckhuysen,  
7 *Insights into the Activity and Deactivation of the Methanol-to-Olefins Process over Different Small-Pore*  
8 *Zeolites As Studied with Operando UV-vis Spectroscopy*. ACS Catalysis, 2017. **7**(6): p. 4033-4046.
- 9 59. Borodina, E., H. Sharbini Harun Kamaluddin, F. Meirer, M. Mokhtar, A.M. Asiri, S. Al-Thabaiti,  
10 S.N. Basahel, J. Ruiz-Martinez, and B. Weckhuysen, *Influence of the reaction temperature on the nature*  
11 *of the active and deactivating species during methanol-to-olefins conversion over H-SAPO-34*. ACS  
12 Catalysis, 2017. **7**(8): p. 5268-5281.
- 13 60. Nijhuis, T.X., S.J. Tinnemans, T. Visser, and B.M. Weckhuysen, *Operando spectroscopic*  
14 *investigation of supported metal oxide catalysts by combined time-resolved UV-VIS/Raman/on-line*  
15 *mass spectrometry*. Physical Chemistry Chemical Physics, 2003. **5**(20): p. 4361-4365.
- 16 61. Bordiga, S., C. Lamberti, F. Bonino, A. Travert, and F. Thibault-Starzyk, *Probing zeolites by*  
17 *vibrational spectroscopies*. Chemical Society Reviews, 2015. **44**(20): p. 7262-7341.
- 18 62. Nachtigall, P., M.R. Delgado, D. Nachtigallova, and C.O. Areán, *The nature of cationic*  
19 *adsorption sites in alkaline zeolites—single, dual and multiple cation sites*. Physical Chemistry Chemical  
20 Physics, 2012. **14**(5): p. 1552-1569.
- 21 63. Almutairi, S.M.T., B. Mezari, E.A. Pidko, P.C.M.M. Magusin, and E.J.M. Hensen, *Influence of*  
22 *steaming on the acidity and the methanol conversion reaction of HZSM-5 zeolite*. Journal of Catalysis,  
23 2013. **307**: p. 194-203.
- 24 64. Gabrienko, A.A., I.G. Danilova, S.S. Arzumanov, L.V. Pirutko, D. Freude, and A.G. Stepanov,  
25 *Direct Measurement of Zeolite Brønsted Acidity by FTIR Spectroscopy: Solid-State <sup>1</sup>H MAS NMR*  
26 *Approach for Reliable Determination of the Integrated Molar Absorption Coefficients*. The Journal of  
27 Physical Chemistry C, 2018. **122**(44): p. 25386-25395.
- 28 65. Dwyer, J., F. Fitch, and E. Nkang, *Dependence of zeolite properties on composition. Unifying*  
29 *concepts*. The Journal of Physical Chemistry, 1983. **87**(26): p. 5402-5404.
- 30 66. Liu, C., G. Li, E.J. Hensen, and E.A. Pidko, *Relationship between acidity and catalytic reactivity*  
31 *of faujasite zeolite: A periodic DFT study*. Journal of Catalysis, 2016. **344**: p. 570-577.
- 32 67. Wang, N., Y. Zhi, Y. Wei, W. Zhang, Z. Liu, J. Huang, T. Sun, S. Xu, S. Lin, and Y. He, *Molecular*  
33 *elucidating of an unusual growth mechanism for polycyclic aromatic hydrocarbons in confined space*.  
34 Nature Communications, 2020. **11**(1): p. 1-12.
- 35 68. Hu, S., J. Shan, Q. Zhang, Y. Wang, Y. Liu, Y. Gong, Z. Wu, and T. Dou, *Selective formation of*  
36 *propylene from methanol over high-silica nanosheets of MFI zeolite*. Applied Catalysis A: General, 2012.  
37 **445-446**: p. 215-220.
- 38 69. Jeon, M.Y., D. Kim, P. Kumar, P.S. Lee, N. Rangnekar, P. Bai, M. Shete, B. Elyassi, H.S. Lee, and  
39 K. Narasimharao, *Ultra-selective high-flux membranes from directly synthesized zeolite nanosheets*.  
40 Nature, 2017. **543**(7647): p. 690.
- 41 70. Mei, C., P. Wen, Z. Liu, H. Liu, Y. Wang, W. Yang, Z. Xie, W. Hua, and Z. Gao, *Selective production*  
42 *of propylene from methanol: Mesoporosity development in high silica HZSM-5*. Journal of Catalysis,  
43 2008. **258**(1): p. 243-249.
- 44 71. Wu, L., V. Degirmenci, P.C.M.M. Magusin, N.J.H.G.M. Lousberg, and E.J.M. Hensen,  
45 *Mesoporous SSZ-13 zeolite prepared by a dual-template method with improved performance in the*  
46 *methanol-to-olefins reaction*. Journal of Catalysis, 2013. **298**: p. 27-40.
- 47 72. Bleken, F.L., S. Chavan, U. Olsbye, M. Boltz, F. Ocampo, and B. Louis, *Conversion of methanol*  
48 *into light olefins over ZSM-5 zeolite: Strategy to enhance propene selectivity*. Applied Catalysis A:  
49 General, 2012. **447-448**: p. 178-185.
- 50 73. Teketel, S., W. Skistad, S. Benard, U. Olsbye, K.P. Lillerud, P. Beato, and S. Svelle, *Shape*  
51 *selectivity in the conversion of methanol to hydrocarbons: the catalytic performance of one-*  
52 *dimensional 10-ring zeolites: ZSM-22, ZSM-23, ZSM-48, and EU-1*. ACS Catalysis, 2012. **2**(1): p. 26-37.



- 1 74. Khare, R., D. Millar, and A. Bhan, *A mechanistic basis for the effects of crystallite size on light*  
2 *olefin selectivity in methanol-to-hydrocarbons conversion on MFI*. Journal of Catalysis, 2015. **321**: p. 23-  
3 31.
- 4 75. Arstad, B. and S. Kolboe, *The reactivity of molecules trapped within the SAPO-34 cavities in the*  
5 *methanol-to-hydrocarbons reaction*. Journal of the American Chemical Society, 2001. **123**(33): p. 8137-  
6 8138.
- 7 76. Bjørgen, M., F. Bonino, B. Arstad, S. Kolboe, K.P. Lillerud, A. Zecchina, and S. Bordiga, *Persistent*  
8 *methylbenzenium ions in protonated zeolites: The required proton affinity of the guest hydrocarbon*.  
9 ChemPhysChem, 2005. **6**(2): p. 232-235.
- 10 77. Goetze, J. and B.M. Weckhuysen, *Spatiotemporal coke formation over zeolite ZSM-5 during the*  
11 *methanol-to-olefins process as studied with operando UV-vis spectroscopy: a comparison between H-*  
12 *ZSM-5 and Mg-ZSM-5*. Catalysis Science & Technology, 2018. **8**(6): p. 1632-1644.
- 13 78. Wang, C., J. Xu, G. Qi, Y. Gong, W. Wang, P. Gao, Q. Wang, N. Feng, X. Liu, and F. Deng,  
14 *Methylbenzene hydrocarbon pool in methanol-to-olefins conversion over zeolite H-ZSM-5*. Journal of  
15 Catalysis, 2015. **332**: p. 127-137.
- 16 79. Palumbo, L., F. Bonino, P. Beato, M. Bjørgen, A. Zecchina, and S. Bordiga, *Conversion of*  
17 *methanol to hydrocarbons: spectroscopic characterization of carbonaceous species formed over H-*  
18 *ZSM-5*. The Journal of Physical Chemistry C, 2008. **112**(26): p. 9710-9716.
- 19 80. Bjørgen, M., S. Svelle, F. Joensen, J. Nerlov, S. Kolboe, F. Bonino, L. Palumbo, S. Bordiga, and U.  
20 Olsbye, *Conversion of methanol to hydrocarbons over zeolite H-ZSM-5: On the origin of the olefinic*  
21 *species*. Journal of Catalysis, 2007. **249**(2): p. 195-207.
- 22 81. Mores, D., E. Stavitski, M.H.F. Kox, J. Kornatowski, U. Olsbye, and B.M. Weckhuysen, *Space-*  
23 *and Time-Resolved In-situ Spectroscopy on the Coke Formation in Molecular Sieves: Methanol-to-Olefin*  
24 *Conversion over H-ZSM-5 and H-SAPO-34*. Chemistry – A European Journal, 2008. **14**(36): p. 11320-  
25 11327.
- 26 82. Li, C., A. Vidal-Moya, P.J. Miguel, J. Dedecek, M. Boronat, and A. Corma, *Selective Introduction*  
27 *of Acid Sites in Different Confined Positions in ZSM-5 and Its Catalytic Implications*. ACS Catalysis, 2018.  
28 **8**(8): p. 7688-7697.
- 29 83. Han, O.H., C.-S. Kim, and S.B. Hong, *Direct Evidence for the Nonrandom Nature of Al*  
30 *Substitution in Zeolite ZSM-5: An Investigation by <sup>27</sup>Al MAS and MQ MAS NMR*. Angewandte Chemie  
31 International Edition, 2002. **41**(3): p. 469-472.
- 32 84. Dědeček, J., Z. Sobalík, and B. Wichterlová, *Siting and distribution of framework aluminium*  
33 *atoms in silicon-rich zeolites and impact on catalysis*. Catalysis Reviews, 2012. **54**(2): p. 135-223.
- 34 85. Wang, S., Y. Chen, Z. Wei, Z. Qin, H. Ma, M. Dong, J. Li, W. Fan, and J. Wang, *Polymethylbenzene*  
35 *or alkene cycle? theoretical study on their contribution to the process of methanol to olefins over H-*  
36 *ZSM-5 zeolite*. The Journal of Physical Chemistry C, 2015. **119**(51): p. 28482-28498.
- 37 86. Sarv, P., C. Fernandez, J.-P. Amoureux, and K. Keskinen, *Distribution of tetrahedral aluminium*  
38 *sites in ZSM-5 type zeolites: An <sup>27</sup>Al (multiquantum) magic angle spinning NMR study*. The Journal of  
39 Physical Chemistry, 1996. **100**(50): p. 19223-19226.
- 40 87. Dědeček, J., M.J. Lucero, C. Li, F. Gao, P. Klein, M. Urbanova, Z. Tvaruzkova, P. Sazama, and S.  
41 Sklenak, *Complex analysis of the aluminum siting in the framework of silicon-rich zeolites. A case study*  
42 *on ferrierites*. The Journal of Physical Chemistry C, 2011. **115**(22): p. 11056-11064.
- 43 88. Kubo, K., H. Iida, S. Namba, and A. Igarashi, *Selective Formation of Light Olefins by Catalytic*  
44 *Cracking of Naphtha Components over ZSM-5 Zeolite Catalysts*. JOURNAL OF THE JAPAN PETROLEUM  
45 INSTITUTE, 2018. **61**(1): p. 10-19.
- 46 89. Imyen, T., W. Wannapakdee, J. Limtrakul, and C. Wattanakit, *Role of hierarchical micro-*  
47 *mesoporous structure of ZSM-5 derived from an embedded nanocarbon cluster synthesis approach in*  
48 *isomerization of alkenes, catalytic cracking and hydrocracking of alkanes*. Fuel, 2019. **254**: p. 115593.
- 49 90. Voogd, P. and H. Van Bekkum, *Limitation of n-hexane and 3-methylpentane conversion over*  
50 *zeolite ZSM-5 by intracrystalline diffusion*. Applied Catalysis, 1990. **59**(1): p. 311-331.
- 51 91. Zhang, M., M. Wang, B. Xu, and D. Ma, *How to Measure the Reaction Performance of*  
52 *Heterogeneous Catalytic Reactions Reliably*. Joule, 2019. **3**(12): p. 2876-2883.

- 1       92. Bleken, F., W. Skistad, K. Barbera, M. Kustova, S. Bordiga, P. Beato, K.P. Lillerud, S. Svelle, and  
2 U. Olsbye, *Conversion of methanol over 10-ring zeolites with differing volumes at channel intersections:  
3 comparison of TNU-9, IM-5, ZSM-11 and ZSM-5*. *Physical Chemistry Chemical Physics*, 2011. **13**(7): p.  
4 2539-2549.
- 5       93. Teketel, S., U. Olsbye, K.-P. Lillerud, P. Beato, and S. Svelle, *Selectivity control through  
6 fundamental mechanistic insight in the conversion of methanol to hydrocarbons over zeolites*.  
7 *Microporous and Mesoporous Materials*, 2010. **136**(1-3): p. 33-41.
- 8       94. Liu, Z., Y. Chu, X. Tang, L. Huang, G. Li, X. Yi, and A. Zheng, *Diffusion dependence of the dual-  
9 cycle mechanism for MTO reaction inside ZSM-12 and ZSM-22 zeolites*. *The Journal of Physical  
10 Chemistry C*, 2017. **121**(41): p. 22872-22882.
- 11       95. Jamil, A.K., O. Muraza, M. Yoshioka, A.M. Al-Amer, Z.H. Yamani, and T. Yokoi, *Selective  
12 production of propylene from methanol conversion over nanosized ZSM-22 zeolites*. *Industrial &  
13 Engineering Chemistry Research*, 2014. **53**(50): p. 19498-19505.
- 14       96. Cnudde, P., R. Demuynck, S. Vandenbrande, M. Waroquier, G. Sastre, and V.V. Speybroeck,  
15 *Light Olefin Diffusion during the MTO Process on H-SAPO-34: A Complex Interplay of Molecular Factors*.  
16 *Journal of the American Chemical Society*, 2020. **142**(13): p. 6007-6017.

17